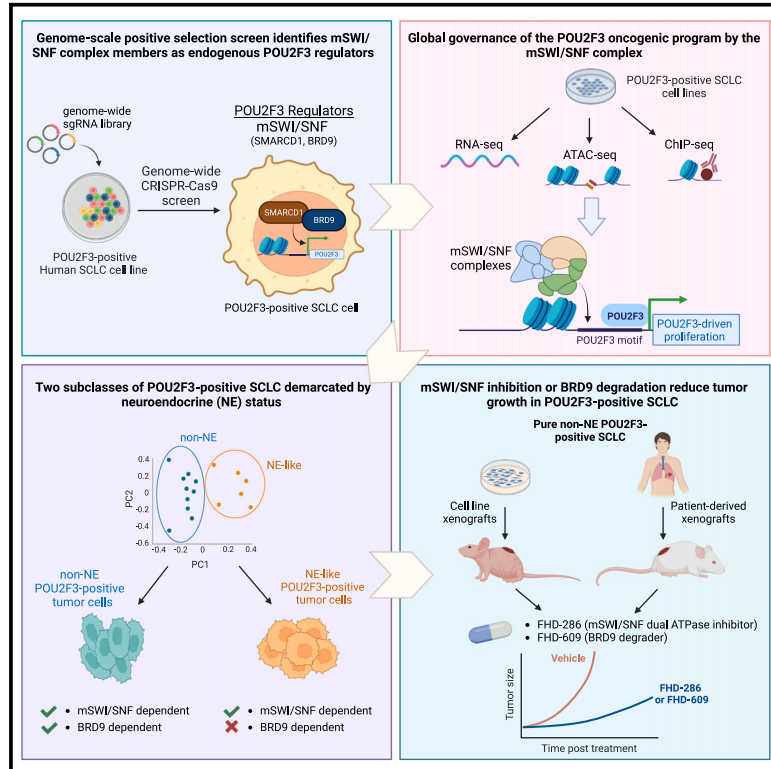


## Mammalian SWI/SNF complex activity regulates POU2F3 and constitutes a targetable dependency in small cell lung cancer

### Graphical abstract



### Authors

Leslie Duplaquet, Kevin So, Alexander W. Ying, ..., Benjamin J. Drapkin, Cigall Kadoch, Matthew G. Oser

### Correspondence

cigall\_kadoch@dfci.harvard.edu (C.K.), matthew\_oser@dfci.harvard.edu (M.G.O.)

### In brief

Duplaquet et al. use positive-selection CRISPR screening to identify that mSWI/SNF chromatin remodeler complexes regulate POU2F3 and its oncogenic program in SCLC and are required for POU2F3<sup>+</sup> SCLC survival. Clinical-grade SMARCA4/2 inhibitors or BRD9 degraders demonstrate efficacy in POU2F3<sup>+</sup> patient-derived and cell line xenograft models.

### Highlights

- A positive selection genome-wide CRISPR-Cas9 screen identifies POU2F3 regulators
- The mSWI/SNF complex maintains POU2F3 and its oncogenic program
- Neuroendocrine (NE) status demarcates two subclasses of POU2F3<sup>+</sup> SCLC
- Non-NE POU2F3<sup>+</sup> SCLCs are highly sensitive to SMARCA4/2 inhibitors and BRD9 degraders

Article

# Mammalian SWI/SNF complex activity regulates POU2F3 and constitutes a targetable dependency in small cell lung cancer

Leslie Duplaquet,<sup>1,15</sup> Kevin So,<sup>2,3,15</sup> Alexander W. Ying,<sup>2,4</sup> Shreoshi Pal Choudhuri,<sup>5,6</sup> Xinyue Li,<sup>1</sup> Grace D. Xu,<sup>2</sup> Yixiang Li,<sup>1</sup> Xintao Qiu,<sup>7</sup> Rong Li,<sup>7</sup> Shilpa Singh,<sup>1</sup> Xiaoli S. Wu,<sup>8</sup> Seth Hamilton,<sup>5,6</sup> Victor D. Chien,<sup>5,6</sup> Qi Liu,<sup>9</sup> Jun Qi,<sup>9</sup> Tim D.D. Somerville,<sup>10</sup> Hillary M. Heiling,<sup>11</sup> Emanuele Mazzola,<sup>11</sup> Yenarae Lee,<sup>4</sup> Thomas Zoller,<sup>10</sup> Christopher R. Vakoc,<sup>8</sup> John G. Doench,<sup>4</sup> William C. Forrester,<sup>10</sup> Tinya Abrams,<sup>10</sup> Henry W. Long,<sup>7</sup> Matthew J. Niederst,<sup>10</sup> Benjamin J. Drapkin,<sup>5,6</sup> Cigall Kadoch,<sup>2,4,12,14,\*</sup> and Matthew G. Oser<sup>1,13,14,16,\*</sup>

<sup>1</sup>Department of Medical Oncology, Dana-Farber Cancer Institute and Brigham and Women's Hospital, Harvard Medical School, Boston, MA 02215, USA

<sup>2</sup>Department of Pediatric Oncology, Dana-Farber Cancer Institute and Harvard Medical School, Boston, MA 02215, USA

<sup>3</sup>Biological and Biomedical Sciences Graduate Program, Harvard Medical School, Boston, MA 02115, USA

<sup>4</sup>Broad Institute of MIT and Harvard, Cambridge, MA 02142, USA

<sup>5</sup>Hamon Center for Therapeutic Oncology Research, University of Texas Southwestern Medical Center, Dallas, TX, USA

<sup>6</sup>Department of Internal Medicine and Simmons Comprehensive Cancer Center, University of Texas Southwestern Medical Center, Dallas, TX, USA

<sup>7</sup>Center for Functional Cancer Epigenetics, Dana-Farber Cancer Institute, Boston, MA 02215, USA

<sup>8</sup>Cold Spring Harbor Laboratory, Cold Spring Harbor, New York, NY 11724, USA

<sup>9</sup>Department of Cancer Biology, Dana-Farber Cancer Institute, Boston, MA 02215, USA

<sup>10</sup>Novartis BioMedical Research, Cambridge, MA 02139, USA

<sup>11</sup>Department of Data Science, Dana-Farber Cancer Institute, Boston, MA 02215, USA

<sup>12</sup>Howard Hughes Medical Institute, Chevy Chase, MD 20815, USA

<sup>13</sup>Department of Medicine, Brigham and Women's Hospital, Harvard Medical School, Boston, MA 02115, USA

<sup>14</sup>Senior authors

<sup>15</sup>These authors contributed equally to this work.

<sup>16</sup>Lead contact

\*Correspondence: [cigall\\_kadoch@dfci.harvard.edu](mailto:cigall_kadoch@dfci.harvard.edu) (C.K.), [matthew\\_oser@dfci.harvard.edu](mailto:matthew_oser@dfci.harvard.edu) (M.G.O.)

<https://doi.org/10.1016/j.ccell.2024.06.012>

## SUMMARY

Small cell lung cancers (SCLCs) are composed of heterogeneous subtypes marked by lineage-specific transcription factors, including ASCL1, NEUROD1, and POU2F3. POU2F3-positive SCLCs, ~12% of all cases, are uniquely dependent on POU2F3 itself; as such, approaches to attenuate POU2F3 expression may represent new therapeutic opportunities. Here using genome-scale screens for regulators of POU2F3 expression and SCLC proliferation, we define mSWI/SNF complexes as top dependencies specific to POU2F3-positive SCLC. Notably, chemical disruption of mSWI/SNF ATPase activity attenuates proliferation of all POU2F3-positive SCLCs, while disruption of non-canonical BAF (ncBAF) via BRD9 degradation is effective in pure non-neuroendocrine POU2F3-SCLCs. mSWI/SNF targets to and maintains accessibility over gene loci central to POU2F3-mediated gene regulatory networks. Finally, clinical-grade pharmacologic disruption of SMARCA4/2 ATPases and BRD9 decreases POU2F3-SCLC tumor growth and increases survival *in vivo*. These results demonstrate mSWI/SNF-mediated governance of the POU2F3 oncogenic program and suggest mSWI/SNF inhibition as a therapeutic strategy for POU2F3-positive SCLCs.

## INTRODUCTION

Small cell lung cancer (SCLC) is a high-grade neuroendocrine cancer that accounts for ~15% of lung cancers,<sup>1–3</sup> driven by loss-of-function (LOF) mutations in tumor suppressor genes *RB1* and *TP53*.<sup>4–6</sup> SCLC are heterogeneous and broadly consist of four molecular subtypes, including the neuroendocrine sub-

types marked by ASCL1 (~60%) and NEUROD1 (~20%), and the non-neuroendocrine subtypes marked by the POU-family transcription factor (TF) POU2F3 (~10–12%) or the inflammatory subtype (~10%).<sup>3,7–10</sup> Notably, the subtypes marked by high expression of lineage-specific TFs ASCL1, NEUROD1, and POU2F3 offer potential therapeutic opportunities as these TFs represent selective dependencies in the SCLCs in which they

are expressed.<sup>11–16</sup> In particular, the POU2F3 SCLC subtype is highly dependent on expression of POU2F3 itself or the recently discovered POU2F3 co-activators OCA-T1 (gene names *C11ORF53/POU2AF2*) or OCA-T2 (gene names *COLCA2/POU2AF3*).<sup>13–16</sup>

POU2F3 (or OCT-11) is an octameric binding TF that canonically binds to the octamer DNA motif ATGCAAAT.<sup>17</sup> SCLCs that express POU2F3 are associated with low expression of neuroendocrine markers.<sup>7</sup> Apart from SCLC and neuroendocrine prostate cancer,<sup>18</sup> expression of POU2F3 is highly tissue restricted and is essential for the development of tuft cells and mucosal epithelial cells.<sup>19</sup> POU2F3-knockout mice are completely viable and only exhibit loss of tuft cells.<sup>20–23</sup> Despite this exquisite cell specificity and likely limited resulting toxicity if targeted, chemical disruption of the POU2F3 TF itself remains an unmet challenge.

Here we use a positive selection CRISPR-Cas9-based screening strategy to identify genes that when inactivated decrease POU2F3 expression in SCLC cellular models. We uncover selective dependencies on the mammalian SWI/SNF (mSWI/SNF or BAF) family of ATP-dependent chromatin remodeling complexes, large multi-subunit assemblies that govern genomic accessibility and gene expression<sup>24</sup> and which are frequently mutated in human cancers.<sup>25</sup> An emerging body of evidence implicates mSWI/SNF complexes in the maintenance and oncogenicity of a range of tumor types,<sup>26–33</sup> which has prompted the development of small molecule inhibitors and degraders that are currently being evaluated in clinical trials<sup>34–36</sup> ([NCT04879017](#) and [NCT04891757](#)). Our findings expand the growing repertoire of cancers in which mSWI/SNF complexes are leveraged to orchestrate oncogenic gene expression and suggest therapeutic opportunities for aggressive POU2F3-positive SCLC.

## RESULTS

### Genome-scale positive selection screen identifies key POU2F3 regulators

We recently developed a positive selection-based screening approach to identify regulators of an oncogene of interest by fusing the oncogene to a modified version of deoxycytidine kinase (oncogene-DCK\*).<sup>37</sup> Here, BVdU selectively kills cells that express oncogene-DCK\*, while cells that downregulate oncogene-DCK\* are BVdU-resistant and survive BVdU treatment (Figure 1A). Early iterations of this assay involved lentiviral overexpression of an oncogene-DCK\* under the control of a ubiquitous promoter (e.g., CMV) in HEK-293T or Jurkat cells,<sup>37</sup> and did not report on endogenous gene regulation. Here we modified the DCK\*/BVdU CRISPR-Cas9 screening approach to identify regulators of endogenous expression of *POU2F3*, a lineage-specific TF oncogene demarcating 10–12% of SCLCs.<sup>3,7,14</sup> To do this, we used CRISPR-Cas9 to knock-in DCK\*, a self-cleaving peptide (P2A), and GFP to create a POU2F3-DCK\*-P2A-GFP fusion in the NCI-H1048 SCLC cell line that expresses and is dependent on POU2F3 (Figure 1B; Table S1).<sup>13,14</sup> Two rounds of fluorescence-activated cell sorting (FACS) for GFP-positive cells obtained a pure population of NCI-H1048 POU2F3-DCK\*-P2A-GFP cells (Figures 1C and S1A). As expected, NCI-H1048 POU2F3-DCK\*-P2A-GFP cells were highly sensitive to BVdU relative to NCI-H1048 parental cells with a large therapeutic win-

dow at 10  $\mu$ M BVdU (Figure 1D). NCI-H1048 cells require POU2F3 for their survival,<sup>14</sup> and therefore one potential obstacle for screening was whether the strong negative selection for sgRNAs targeting POU2F3 or its regulators outweigh BVdU-induced positive selection. To address this, we used CRISPR to inactivate POU2F3 in NCI-H1048 POU2F3-DCK\*-P2A-GFP cells. As expected, POU2F3 CRISPR inactivation decreased proliferation and induced apoptosis (Figures S1B–S1D). Despite these loss-of-fitness phenotypes, POU2F3 knockout was partially maintained over a 15 day time window and caused partial BVdU resistance (Figures S1B and S1E) demonstrating that strong positive selection with BVdU could overcome the negative selection after POU2F3 loss. Consistent with these results, DCK CRISPR inactivation also caused partial BVdU resistance together demonstrating the BVdU anti-proliferative impact was due to POU2F3-DCK\* expression (Figures S1F and S1G).

To identify endogenous regulators of POU2F3, we next subjected NCI-H1048 POU2F3-DCK\*-P2A-GFP cells to CRISPR-Cas9 BVdU resistance screens using the genome-wide Brunello sgRNA library containing 77,741 targeting sgRNAs and 1,000 control sgRNAs at an MOI of 0.5<sup>38</sup> (Figure 1E). Following transduction and selection, all cells were pooled and an early time point (day 9) was harvested. Remaining cells were split into 2 arms (10  $\mu$ M BVdU or untreated) and grown in either BVdU or untreated for 7 days (day 16) at which point the cells were harvested for genomic DNA was isolation and deep sequencing.

Analysis of changes in sgRNA abundance identified several sgRNAs exhibiting robust enrichment in both biological replicates in BVdU versus untreated samples, demonstrating technical success (Figures S1H–S1J; Table S2). Importantly, among the top-scoring guides were those corresponding to *DCK* and *POU2F3* (Figure S1J). Notably, gene level analyses comparing BVdU and untreated conditions at day 16 highlighted several top-scoring sgRNAs with scores at or near those of *DCK* and *POU2F3*, including those targeting chromatin regulatory genes (*MED19*, *EP300*, and *KAT7*), signaling pathway members (*IPPK*), and members of the mSWI/SNF (BAF) family of ATP-dependent chromatin remodeling complexes, particularly the non-canonical BAF (ncBAF) complex<sup>39</sup> including *SMARCD1* and *BRD9* (Figure 1F; Table S2).

### Non-canonical BAF complexes promote POU2F3 expression and proliferation in POU2F3-positive SCLC

To validate our findings, CRISPR-based inactivation was performed on several highly significant top-enriched hits. *SMARCD1*, *EP300*, *MED19*, *IPPK*, and *KAT7* depletion all markedly reduced total POU2F3 protein levels and proliferation in NCI-H1048 SCLC cells (Figures 2A and S2A; Table S2). We then sought to determine which enriched hits represented selective dependencies for POU2F3-positive SCLC. We analyzed DepMap (Project Achilles, Broad Institute) datasets (23Q2 release) reporting on genome-scale CRISPR-Cas9 knockout screens performed across >1,000 cancer cell lines<sup>40</sup> including 23 SCLC cell lines in total and all four POU2F3-positive cell lines (NCI-H1048, NCI-H211, NCI-H526 and COR-L311). POU2F3-positive SCLC lines were significantly dependent on ncBAF components *SMARCD1* and *BRD9* and the conserved mSWI/SNF ATPase subunit, *SMARCA4*, relative to other SCLCs and all other cancer cell lines (Figures 2B, 2C, and S2B–S2F; Table S3). In contrast to

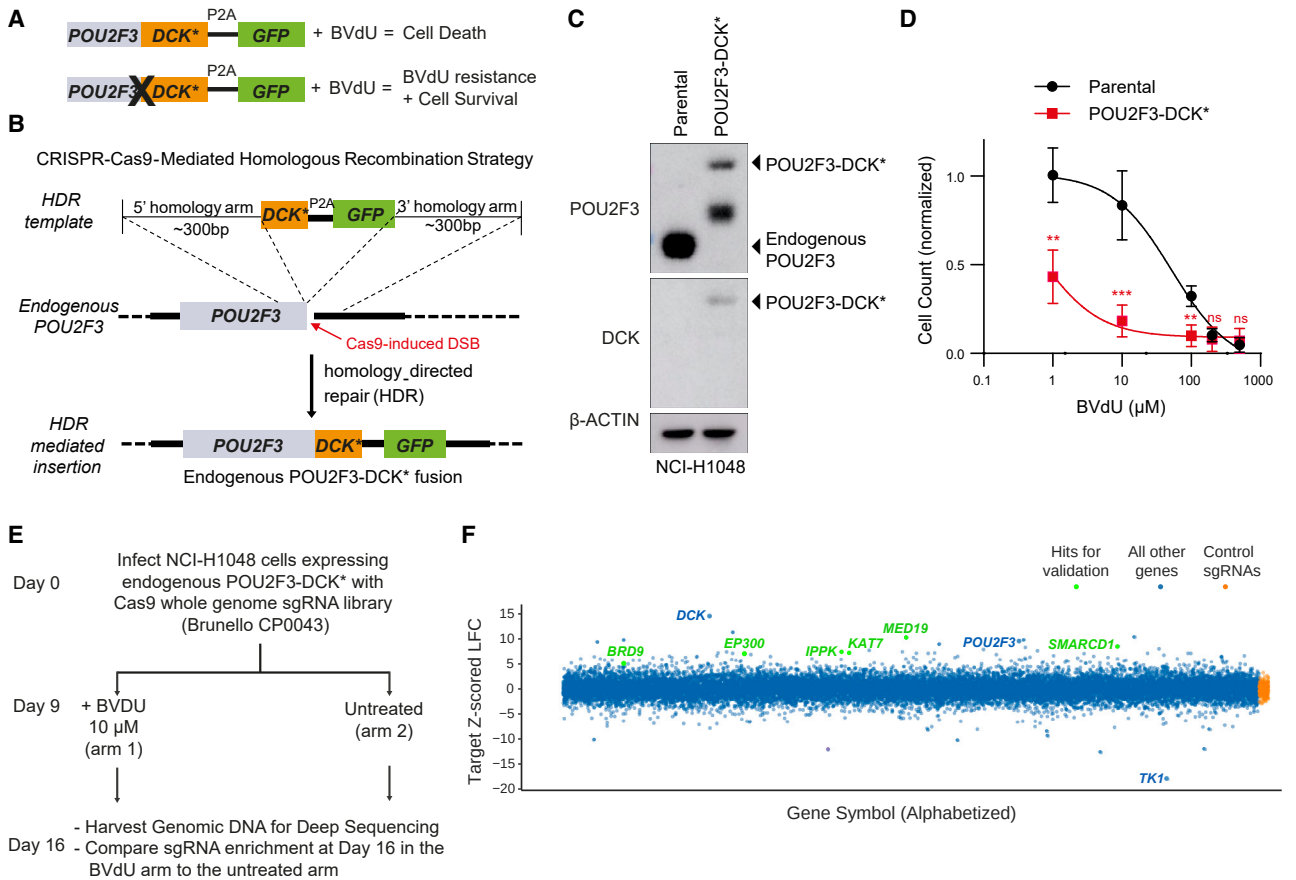


**Figure 1. Genome-scale positive selection screen identifies key POU2F3 regulators**

(A) Schema for positive selection assay to identify regulators of POU2F3 where  $DCK^*$  variant allows the incorporation of the cytotoxic BVdU metabolites which are otherwise not toxic to wild-type cells.  $DCK^*$ , variant of deoxycytidine kinase; BVdU, bromovinyl deoxyuridine. (B) CRISPR-Cas9-mediated homologous recombination strategy used to knock-in (KI)  $DCK^*$  and GFP (linked by P2A) into the endogenous POU2F3 locus of human NCI-H1048 SCLC cell line. These KI cells endogenously express POU2F3- $DCK^*$ -P2A-GFP chimeric fusion protein. (C) Immunoblot analysis of NCI-H1048 engineered to endogenously express POU2F3- $DCK^*$  using the strategy in (B). (D) BVdU dose response assays of the indicated cell lines from (C) treated with BVdU for 7 days showing viable cell counts relative to DMSO control.  $n = 4$  biological replicates. \*\* $p < 0.01$ , \*\*\* $p < 0.001$  using a 2-tailed unpaired t test. Error bars represent mean  $\pm$  SEM. (E) Schema of the CRISPR-Cas9 positive selection screen performed in NCI-H1048 POU2F3- $DCK^*$ -P2A-GFP cells transduced with the whole genome Brunello sgRNA library. Following selection, cells were treated with BVdU (10  $\mu$ M) or untreated for 7 days and harvested to extract genomic DNA for deep sequencing. (F) Apron analysis from the positive-selection CRISPR-Cas9 screen in (E) comparing BVdU vs. untreated NCI-H1048 POU2F3- $DCK^*$ -P2A-GFP cells.  $n = 2$  biological replicates. Enriched hits for validation are marked in green.  $DCK$  and  $POU2F3$  are labeled as positive controls for enrichment.  $TK1$  is labeled as a positive control for depletion as  $TK1$  inactivation hypersensitizes cells to BVdU. See also [Figure S1](#) and [Tables S1](#) and [S2](#).

mSWI/SNF components, POU2F3 dependency did not significantly correlate with the dependencies of other hits validated to impact POU2F3 expression ( $EP300$ ,  $MED19$ ,  $IPPK$ , and  $KAT7$ ) ([Figures S2C–S2G](#)).

We therefore focused on mSWI/SNF, including ncBAF, complexes, especially given recently-achieved pharmacologic targeting of these remodelers. Multiple sgRNAs targeting both SMARCD1 and BRD9 significantly reduced POU2F3 protein levels and attenuated NCI-H1048 proliferation nearly to levels achieved by targeting POU2F3 itself ([Figures 2D–2F](#)). Further, CRISPR-mediated suppression of  $GLTSCR1$  ( $BICRA$ ) and  $GLTSCR1L$  ( $BICRAL$ ), the nucleating paralog subunits of ncBAF complexes, similarly attenuated proliferation of NCI-H1048 cells ([Figures 2G](#) and [2H](#)). Proliferative inhibition was further accentuated upon concomitant loss of both  $GLTSCR1/1L$  paralogs,

which eliminates ncBAF complex assembly.<sup>41</sup> Together these data highlight that ncBAF complex integrity is required to maintain POU2F3 expression and proliferation in NCI-H1048 SCLC cells.

### Disruption of pan-mSWI/SNF ATPase and ncBAF-specific componentry attenuates SCLC proliferation

Given our aforementioned findings, we next asked whether small molecules that modulate mSWI/SNF complex activity or assembly impact POU2F3 expression and proliferation of POU2F3-positive SCLCs. We employed two recently-discovered clinical-grade small molecules: FHD-609,<sup>42</sup> a VHL-based small molecule degrader of the BRD9 ncBAF complex subunit; and FHD-286,<sup>43</sup> a small molecule inhibitor of the SMARCA4/SMARCA2 mSWI/SNF ATPase subunits ([Figure 3A](#)). Notably, BRD9 degradation

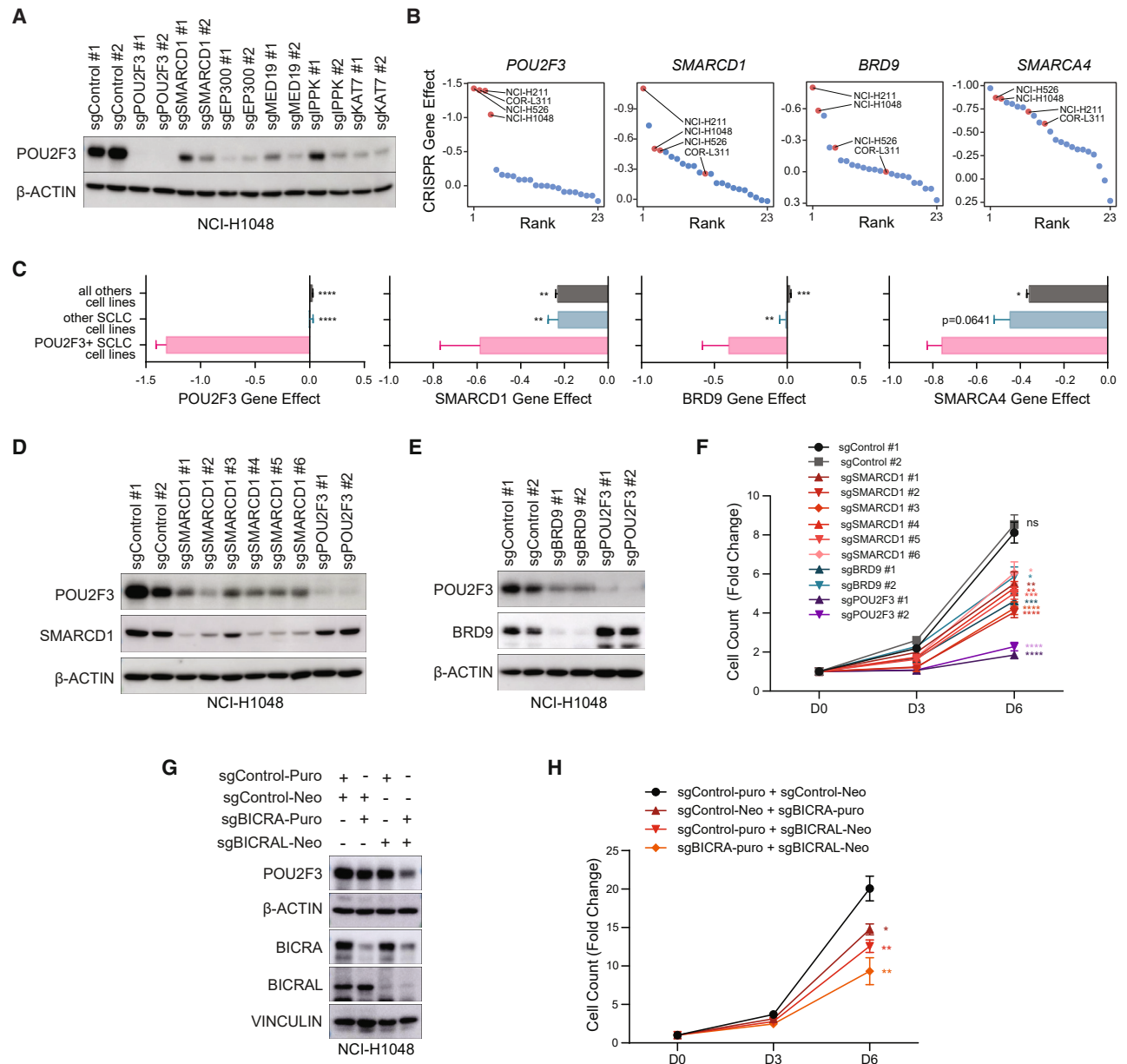


**Figure 2. Non-canonical BAF (ncBAF) complexes regulate POU2F3 expression and proliferation in POU2F3-positive SCLC**

(A) Immunoblot analysis of parental NCI-H1048 cells transduced with sgRNAs targeting genes that scored as candidate POU2F3 regulators or non-targeting controls (sgControl). Immunoblotting was performed 6 days after transduction and is representative of 4 biological replicates.

(B) Cell line rank vs. CRISPR gene effect for *POU2F3*, *SMARCD1*, *BRD9*, and *SMARCA4* of the 23 SCLC cell lines included in the dependency map.

(C) CRISPR gene effect of *POU2F3*, *SMARCD1*, *BRD9*, and *SMARCA4* comparing POU2F3-positive SCLC lines vs. all other SCLC lines vs. all other cancer cell lines from the dependency map.  $n = 4$  POU2F3-expressing SCLC cell lines,  $n = 19$  other SCLC cell lines,  $n = 1,072$  all other cancer cell lines.

(D–H) Immunoblot analysis (D, E, and G) and quantification of cell counts 3 and 6 days after plating (F and H) of NCI-H1048 parental cells transduced with the indicated sgRNAs targeting *SMARCD1*, *BRD9*, *BICRA/BICRAL*, or non-targeting controls (sgControl). In (D–F), POU2F3 sgRNAs are included as benchmark controls. For (G) and (H), sgControl #1 was used. Cell counts are plotted as fold change relative to day 0.  $n = 6$  biological replicates for F and  $n = 4$  biological replicates for (H). For all panels,  $*p < 0.05$ ,  $**p < 0.01$ ,  $***p < 0.001$ ,  $****p < 0.0001$  using a 2-tailed unpaired t test. Error bars represent mean  $\pm$  SEM. See also Figure S2 and Tables S2 and S3.

using FHD-609 and two additional BRD9 degraders, WA-68-VQ71 and dBRD9A, reduced POU2F3 protein levels and attenuated proliferation of the two POU2F3-positive SCLC lines (NCI-H1048 and NCI-H211) with EC50s in the low nanomolar range, but did not have an impact on NCI-H526 and COR-L311

POU2F3-positive SCLC lines (Figures 3B–3D and S3A–S3D). This distinction between POU2F3-positive lines was corroborated by DepMap, in which NCI-H1048 and NCI-H211 cells demonstrated greater BRD9 dependency (Figure 2B). Further, inhibition of mSWI/SNF ATPase activity using FHD-286 resulted

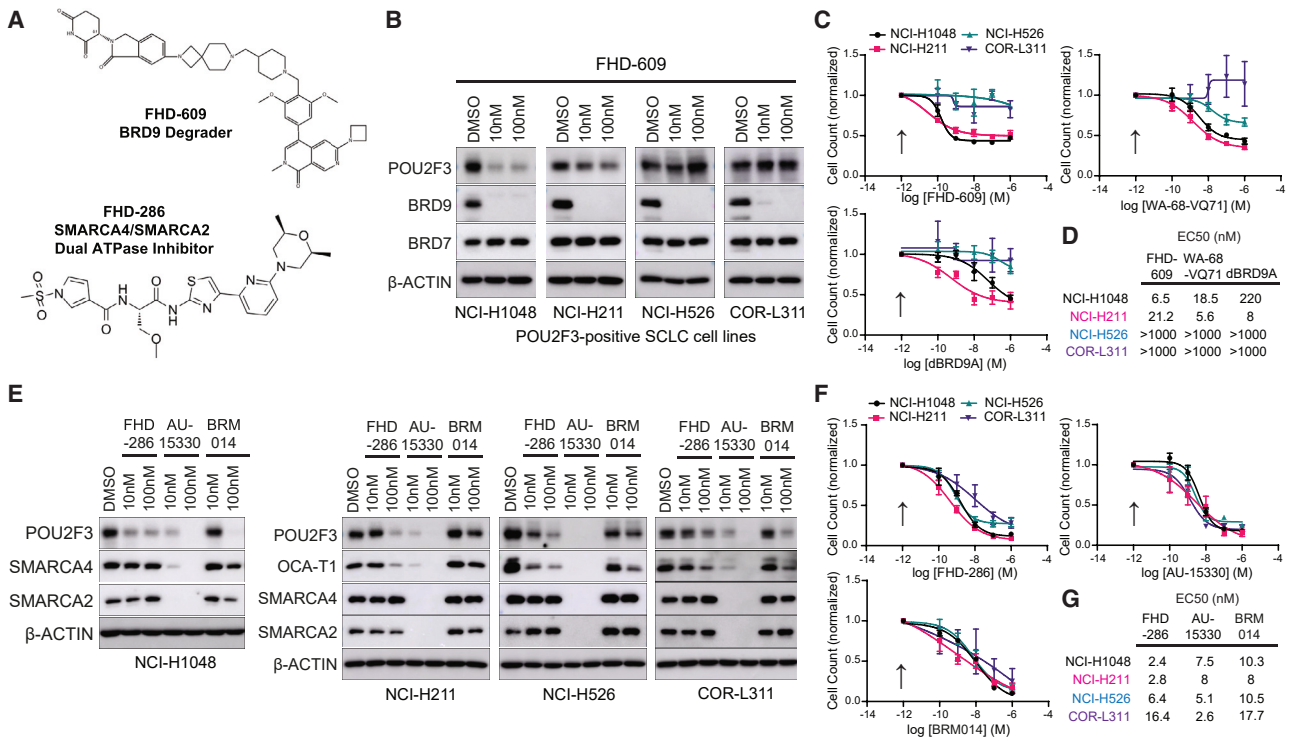


**Figure 3. Disruption of pan-mSWI/SNF ATPase and ncBAF-specific componentry attenuates SCLC proliferation**

(A) Structure of the clinical-grade BRD9 degrader FHD-609 and clinical grade FHD-286 SMARCA4/2 ATPase inhibitor.  
 (B) Immunoblot analysis of the indicated POU2F3-expressing human SCLC lines after treatment with FHD-609 or DMSO for 3 days.  
 (C) Dose response assays of POU2F3-expressing human SCLC cell lines treated for 6 days with 3 different BRD9 degraders: FHD-609, WA-68-VQ71, or dBRD9A.  $n = 3$  biological replicates.  
 (D) Table showing calculated EC50s from dose response assays in (C).  
 (E) Immunoblot analysis of NCI-H1048, NCI-H211, NCI-526, and COR-L311 cells after treatment with SMARCA4/2 dual inhibitors (FHD-286 or BRM014) or the SMARCA4/2 degrader (AU-15330) or DMSO for 3 days.  
 (F) Dose response assays of POU2F3-expressing human SCLC cell lines treated for 6 days with FHD-286, AU-15330, or BRM014.  $n = 3$  biological replicates.  
 (G) Table showing EC50s from dose response assays in (F). For all doses response assays, cell counts are normalized to DMSO. Arrows in (C) and (F) indicate DMSO-treated sample which was used for normalization. Error bars represent mean  $\pm$  SEM. See also [Figure S3](#).

in dramatic reduction of POU2F3 levels and proliferation with EC50s in the low nanomolar range across all 4 POU2F3-positive SCLCs (Figures 3E–3G). These data were further validated using a SMARCA4/2 degrader, AU-15330,<sup>26</sup> and a second ATPase inhibitor, BRM014<sup>36,44</sup> (Figures 3E–3G). Overall, FHD-286 and FHD-609 did not induce apoptosis in POU2F3-positive lines with the exception being FHD-286 in NCI-H1048 cells (Figures S3E and S3F). Treatment with either FHD-286 or FHD-609 did not induce changes to mSWI/SNF subunit protein-level abundance (other than BRD9 for FHD-609, as expected) (Figure S3G). Of note, subunit protein-level abundance was similar across all POU2F3-positive lines except for NCI-H1048 cells in which ARID1A (cBAF-specific subunit) levels were reduced (Figure S3H), which has been correlated with increased ncBAF subunit abundance and function.<sup>39,45</sup> These antiproliferative phenotypes were selective for POU2F3-positive SCLC lines as SCLC cell lines of the ASCL1 and NEUROD1 subtypes were relatively insensitive to BRD9 degraders, WA-68-VQ71 and FHD-609, and SMARCA4/2 inhibitors FHD-286 and BRM014, with EC50s  $> 1 \mu\text{M}$  (Figures S3I and S3J). Treatment with these agents did not decrease ASCL1 or NEUROD1 protein levels except for modest changes in NEUROD1 in NCI-H82 cells

and modest changes in ASCL1 in NCI-H1836 cells upon SMARCA4/2 inhibition (Figures S3K–S3N). Together, these data underscore critical oncogenic maintenance functions of mSWI/SNF family complexes in POU2F3-expressing SCLC. In addition, while all POU2F3-positive SCLC lines evaluated were dependent on mSWI/SNF complex activity, these results indicate that further subdivision of POU2F3 SCLCs can demarcate sensitivity to ncBAF complex disruption.

### Neuroendocrine status demarcates two subclasses of POU2F3-positive SCLC and predicts sensitivity to ncBAF disruption

We next sought to characterize the molecular differences between POU2F3-positive SCLC lines that do and do not exhibit sensitivity to ncBAF disruption. Unsupervised clustering of gene expression (RNA sequencing [RNA-seq]) across the four cell lines indicated clear segregation in expression profiles of the NCI-H1048 and NCI-H211 cell lines and the NCI-H526 and COR-L311 cell lines (Figure 4A). Notably, neuroendocrine genes including *SYN* (synaptophysin), *INSM1*, *CHGA* (chromogranin A), *SEZ6*, and *ACTL6B* nearly exclusively demarcated the NCI-H526 and COR-L311 cell lines that were non-responsive to ncBAF

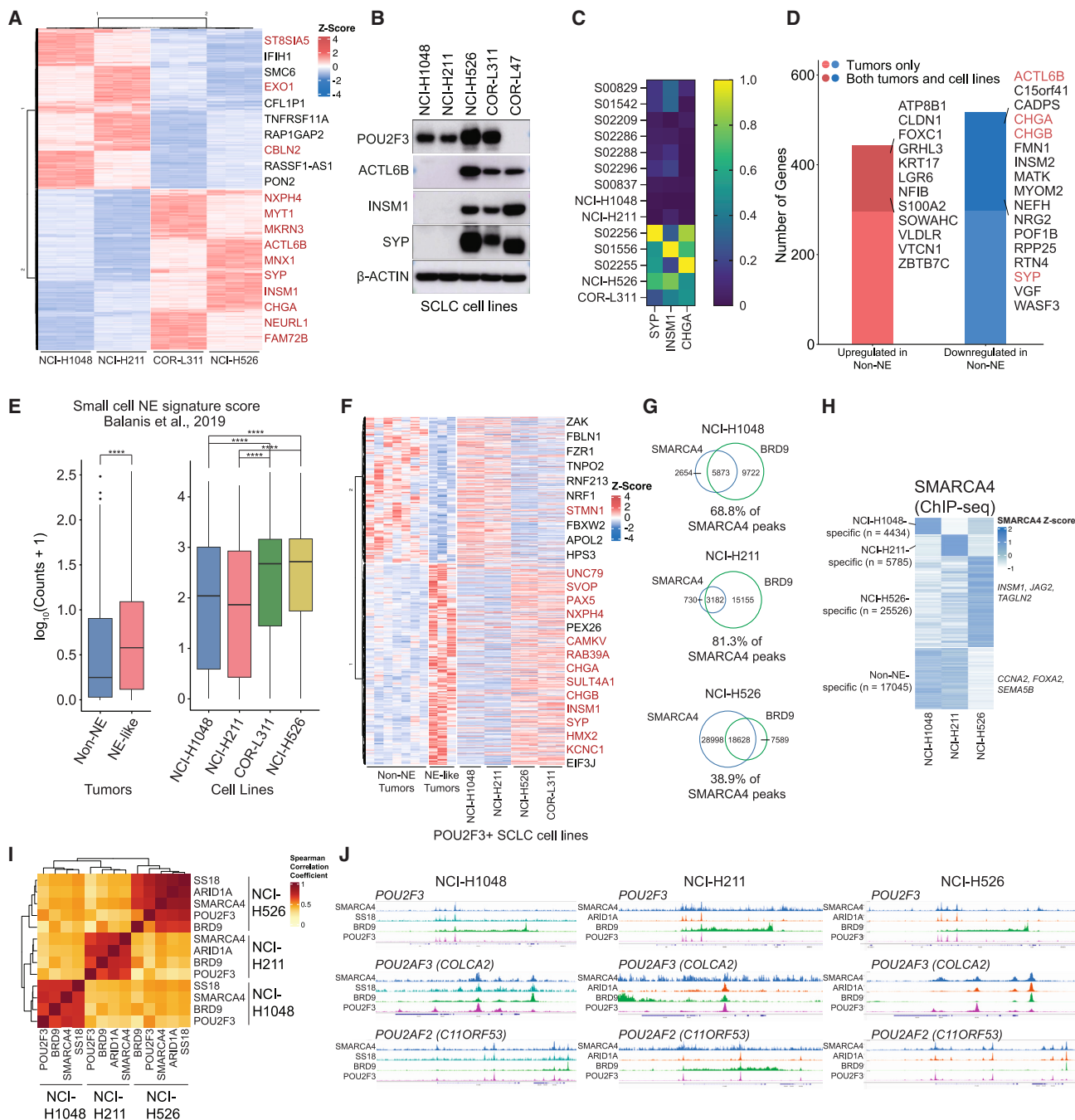


**Figure 4. Subclassification of POU2F3-positive SCLCs by their neuroendocrine status and sensitivity to ncBAF disruption**

(A) Heatmap depicting top 10% up- and downregulated genes between NE-like and non-NE cell lines, by Z score normalized expression. Red indicates genes as being in the top 500 genes in the Balanis et al., 2019 SCLC signature. <sup>46</sup>

(B) Immunoblot for ACTL6B, INSM1, and SYP NE markers from SCLC cell lines.

(C) Heatmap depicting gene expression of *SYP*, *INSM1*, and *CHGA* in SCLC primary tumors and cell lines. Color scale represents normalized mRNA expression.

(D) Stacked bar graph depicting genes selectively up- and downregulated in non-NE and NE-like SCLC primary tumors; dark red and dark blue indicate those genes overlapping genes selectively up- and downregulated in SCLC cell lines. Red indicates NE genes.

(E) Boxplot of log-transformed counts for top 500 SCNC signature genes in both George et al. 2015 mRNA data from SCLC tumors with POU2F3 expression and POU2F3-positive cell lines. Pairwise t test was conducted to test for significance. \* $p < 0.05$ , \*\* $p < 0.01$ , \*\*\* $p < 0.001$ , \*\*\*\* $p < 0.0001$ . The centerlines indicate the median. The box limits indicate the 25% and 75% percentiles. The whiskers indicate 25% percentile -1.5\*IQR and 75% percentile +1.5\*IQR. IQR = 75% percentile value - 25% percentile value.

(legend continued on next page)

inhibition, while those lines responding showed markedly reduced neuroendocrine gene expression (Figure 4A). Pure non-neuroendocrine (non-NE) cell lines NCI-H1048 and NCI-H211 showed genes such as *IFIH1* and *TNFRSF11A* uniquely upregulated and were enriched for immune signatures including interferon alpha and gamma response and IL2 and IL6 JAK-STAT signaling relative to the neuroendocrine (NE)-like POU2F3-positive cell lines, which were more enriched in oxidative phosphorylation, UV response, and pancreas beta cell signatures (Figure S4A). Validation of selected NE-associated genes at the total protein level indicated clear separation between the purely non-NE and NE-like cell lines, with NE-like cell lines more closely mimicking SCLCs lacking POU2F3 expression (e.g., COR-L47) (Figure 4B).

We next integrated these data with RNA-seq data from George et al. containing 12 primary SCLC tumors with POU2F3 expression<sup>4</sup> (Figure S4B; Table S4) to ask whether these two subsets exist within POU2F3-positive human SCLC, and to define gene signatures shared between primary tumors and cell line models. Of note, key NE marker genes such as *SYP*, *INSM1*, and *CHGA* were expressed exclusively in the two NE-like cell lines and demonstrated much higher expression in a subset of  $n = 3$  POU2F3-positive primary tumors (Figures 4C and S4C–S4E). Indeed, principal-component analysis (PCA) confirmed several NE features, among others, driving this separation (Figure S4E). Gene expression analyses integrating both cell lines and primary tumor data indicated that among differentially expressed genes in primary SCLC tumors, 37% upregulated and 41% downregulated genes mirrored those selectively up or downregulated in our cell line models (Figure 4D). Further, using a neuroendocrine signature gene set of 250 total genes,<sup>46</sup> these two subgroups are even more clearly demarcated, indicative of NE features being the primary driver of the separation within the POU2F3-positive SCLC subtype (Figures 4E, 4F, and S4F). We also observed non-NE and NE-like POU2F3-positive human SCLC tumors using RNA-seq data from a recently published study that included 16 POU2F3-positive SCLCs<sup>47</sup> (Figures S4G–S4I). While expression of NE genes was strongly correlated with BRD9 degrader insensitivity, CRISPR inactivation of neuroendocrine lineage TF *INSM1* or the neural/neuroendocrine lineage mSWI/SNF complex member *ACTL6B* was not sufficient to induce BRD9 degrader sensitivity in NCI-H526 and COR-L311 POU2F3-positive NE-like lines (Figures S4J–S4Q).

We next performed chromatin immunoprecipitation sequencing (ChIP-seq) studies to characterize the occupancy of mSWI/SNF complexes (via SMARCA4 [BRG1], SS18, ARID1A, and BRD9) and the POU2F3 TF. Globally, BRD9 exhibited the lowest overlap with SMARCA4 sites genome-wide in the BRD9 degradation-insensitive cell line, NCI-H526, relative to two BRD9 degradation-sensitive cell lines, NCI-H1048 and NCI-

H211 (Figure 4G). We identified a number of SMARCA4 sites that were specific to the two BRD9 degradation-sensitive cell lines and sites specific to the BRD9 degradation-insensitive cell line and identified nearby genes (Figure 4H). Further, BRD9 was most weakly associated with POU2F3 and SMARCA4 genome-wide binding including reduced occupancy at the *POU2F3* and *POU2AF2* loci in NCI-H526 cells relative to NCI-H1048 and NCI-H211 cells (Figures 4I, 4J, and S4R).

We next aimed to define the impact of either BRD9 degradation (FHD-609) or SMARCA4/2 ATPase inhibition (FHD-286) on chromatin accessibility, histone landscape features, and subtype-specific gene expression (Figure 5A). NCI-H1048 and NCI-H211 cells were treated with FHD-609 (100 nM) or DMSO for 72 h. Gene expression (RNA-seq) analyses indicated top downregulated pathways in both lines included MYC target genes, G2M checkpoint, and E2F targets, in agreement with the strong antiproliferative impact of FHD-609 (Figures 5B, S5A–S5C, 2, and 3). Common differentially expressed genes upon ncBAF disruption (FHD-609 treatment) included *NTRK2* and *TMPPRSS15* (Figure 5C). To begin to define the underlying mechanisms, we evaluated changes in mSWI/SNF chromatin occupancy and chromatin accessibility using ChIP-seq and ATAC-seq, respectively. Treatment with FHD-609 in NCI-H1048 cells resulted in substantial reduction in SMARCA4 occupancy genome-wide and BRD9 chromatin binding, as expected given its degradation (Figures 5D and 5E). POU2F3 occupancy was modestly reduced at these sites (Figure 5E). SS18 was also modestly reduced in accordance with SS18 integrating into ncBAF and cBAF complexes (Figure 5E).<sup>41</sup> Hypergeometric Optimization of Motif EnRichment (HOMER) analysis identified POU2F3 and POU homeobox motifs as the most enriched TF motifs associated with sites with SMARCA4 loss (Figure 5F). Globally, in both NCI-H1048 and NCI-H211 cells, FHD-609 treatment revealed substantial changes, both decreases and increases, in accessibility genome-wide (Figures 5G and 5H). Notably, sites with reduction in chromatin accessibility upon FHD-609 treatment exhibited preferential enrichment for POU2F3 DNA-binding motifs (Figures 5I and S5D). Finally, we integrated these ATAC-seq and RNA-seq data to identify genes with nearby changes in accessibility (putative primary genes) and those without (putative secondary/downstream genes), finding that 81% and 36% of significantly downregulated genes were attributed to reduced nearby chromatin accessibility upon ncBAF disruption, respectively (Figure S5E). Of note, among genes that we had defined as unique to non-NE lines (Figures 4A, 4B, and 4E), treatment with FHD-609 more significantly changed both accessibility and gene expression of those targets (Figure 5J). Taken together, these data highlight the impact of FHD-609-mediated ncBAF disruption on mSWI/SNF and POU2F3 binding, and on chromatin accessibility of the key

(F) Heatmap (Z score) showing top up- and downregulated genes in NE-like and non-NE primary tumors and cell lines. Genes bolded are those that overlap with the NE signature from Balanis et al., 2019. Red indicates NE genes.

(G) Venn diagrams showing overlap between BRD9 and SMARCA4 peaks in NCI-H1048, NCI-H211, and NCI-H526 cells.

(H) Heatmap showing SMARCA4 ChIP-seq signal across cell lines in categories indicated.

(I) Spearman correlation coefficient heatmap with clustering performed across all ChIP-seq experiments (peaks) for SMARCA4, BRD9, and POU2F3 peaks in NCI-H1048, NCI-H211, and NCI-H526 cells.

(J) Chromatin targeting (ChIP-seq for SMARCA4 [BRG1], SS18, ARID1A, BRD9, and POU2F3) at the *POU2F3*, *POU2AF3* (*COLCA2*), and *POU2AF2* (*C11ORF53*) loci in NCI-H1048, NCI-H211, and NCI-H526 cells. See also Figure S4 and Table S4.

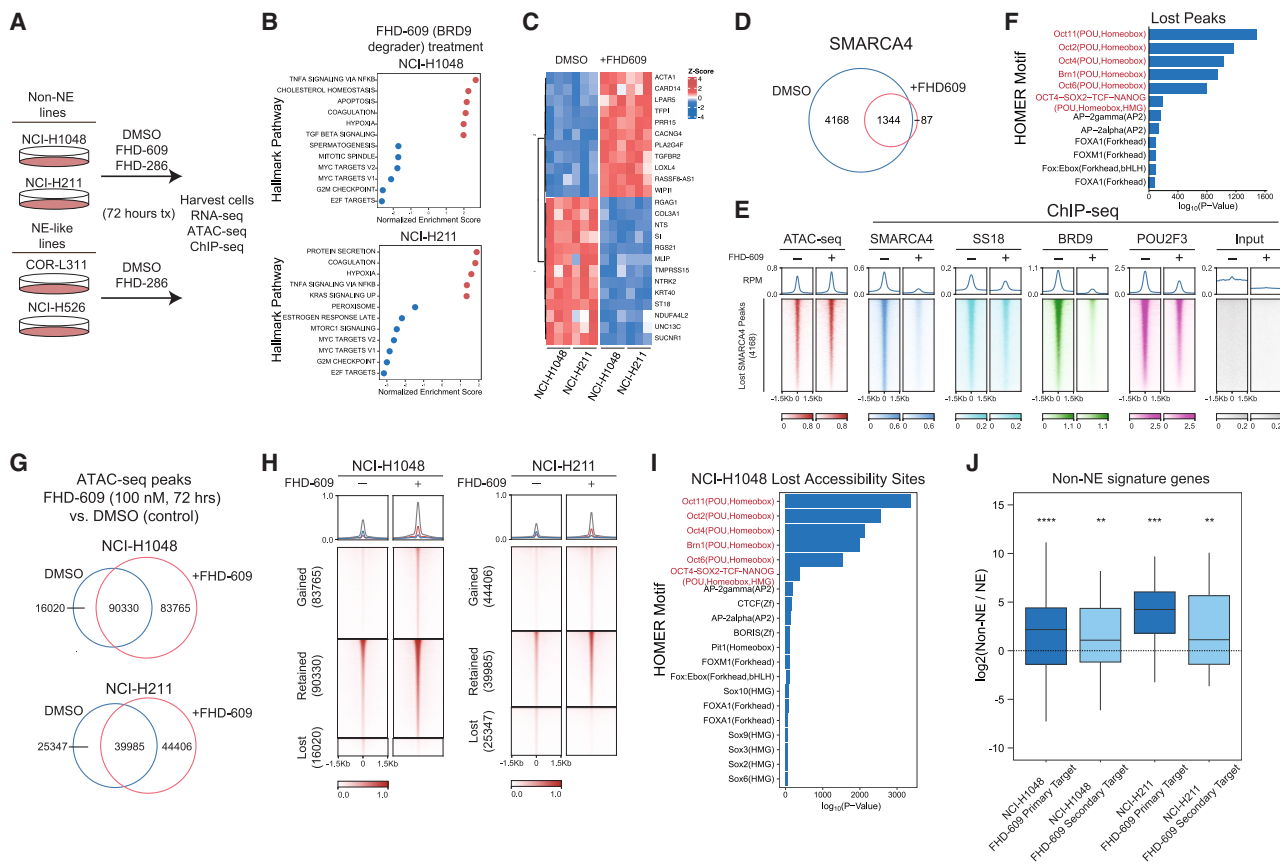


**Figure 5. ncBAF disruption impacts non-NE-specific chromatin and gene regulation in POU2F3-positive SCLC**

(A) Schematic depicting experimental strategy to evaluate mSWI/SNF modulatory small molecules in SCLC cell line models.  
 (B) Dot plot depicting Gene Set Enrichment Analysis (GSEA) normalized enrichment scores (NES) for Hallmark pathways in FHD-609 versus control-treated cells.  
 (C) Heatmap depicting upregulated and downregulated genes shared between non-NE SCLC cell lines by differential gene analysis. Expression counts were Z score normalized by cell line.  
 (D) Venn diagram depicting overlap between SMARCA4 ChIP-seq peaks in FHD-609-treated NCI-H1048 cells and control.  
 (E) Heatmaps depicting chromatin accessibility and SMARCA4, SS18, BRD9, POU2F3 ChIP-seq peak signal performed over lost SMARCA4 sites from (D); input shown as control.  
 (F) Motif enrichment analysis performed over lost SMARCA4 peaks from (D).  
 (G) Venn diagram depicting overlap between ATAC-seq peaks in FHD-609-treated cells and DMSO control.  
 (H) Heatmap showing gained, lost, and retained accessible peaks by ATAC-seq upon FHD-609 treatment in NCI-H1048 and NCI-H211 cells.  
 (I) HOMER motif enrichment analysis performed on sites with lost accessibility upon FHD-609 treatment in NCI-H1048 cells.  
 (J) Non-NE signature genes in primary and secondary target genes identified by integrative ATAC-seq and RNA-seq analyses in non-NE SCLC cell lines treated with FHD-609. The centerlines indicate the median. The box limits indicate the 25% and 75% percentiles. The whiskers indicate 25% percentile  $-1.5 \times$  IQR and 75% percentile  $+1.5 \times$  IQR. IQR = 75% percentile value  $-$  25% percentile value.  $p$  values are indicated and were calculated using Student's 1-tailed t test with Benjamini-Hochberg corrected  $p$ -values reported. \* $p < 0.05$ , \*\* $p < 0.01$ , \*\*\* $p < 0.001$ , \*\*\*\* $p < 0.0001$ . See also Figure S5.

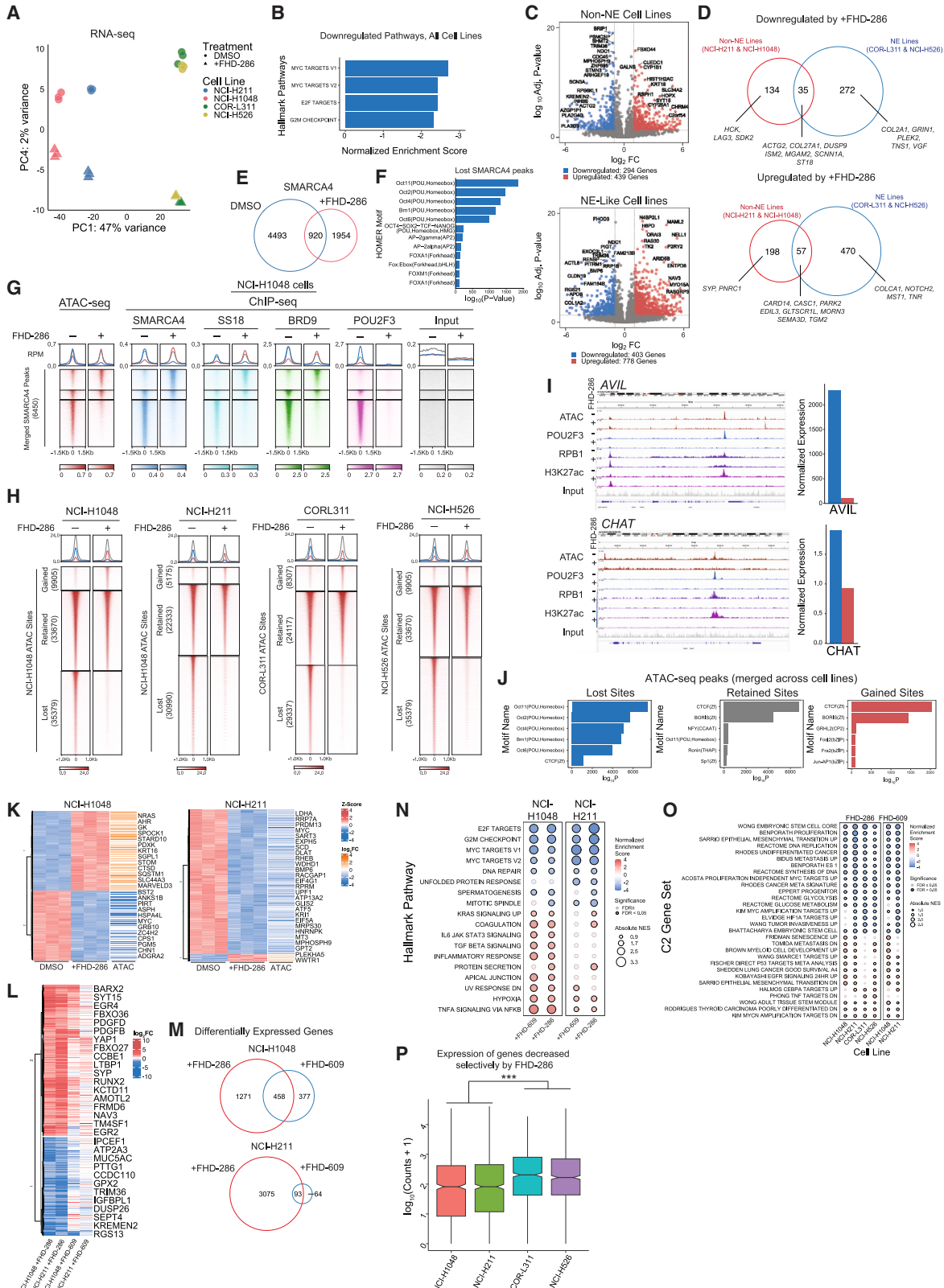
pathways contributing to the maintenance of non-NE POU2F3-positive SCLC.

### mSWI/SNF ATPase inhibition attenuates distinct oncogenic gene regulatory networks mediated by distinct complexes

Given that all POU2F3-positive cell lines exhibited sensitivity to pan-mSWI/SNF ATPase inhibitors, we next sought to evaluate the impact of FHD-286 SMARCA4/2 inhibition across cell lines on gene and chromatin accessibility signatures and define its effect on genes that were impacted by ncBAF-disruption (FHD-609). In line with the antiproliferative impact of FHD-286 (Figure 3), MYC targets, E2F targets, and G2M checkpoint genes

were significantly downregulated across all four SCLC lines following FHD-286 treatment (Figures 6A, 6B, and S6A–S6D). The overall impact on differential gene expression was larger relative to FHD-609 in the non-NE SCLC cell lines, with over 1,000 genes differentially down- and upregulated (Figures 6C and S6A). We identified largely separate groups of genes downregulated and upregulated by FHD-286 in non-NE and NE-like cell lines; however, genes such as *DUSP9*, *COL27A1*, and *MGAM2* were concordantly downregulated and *CARD14*, *MORN3*, and *TGM2* were concordantly upregulated in all cell lines (Figure 6D).

Importantly, treatment with FHD-286 resulted in substantial losses in global SMARCA4 (mSWI/SNF) chromatin binding,



(legend on next page)

particularly over POU2F3 motifs (Figures 6E and 6F). Sites with reductions in SMARCA4 occupancy exhibited marked reduction in all mSWI/SNF complex subunit binding, including SS18 and BRD9, and an almost complete disappearance of POU2F3 at lost sites and throughout the genome (including at sites with gained and retained occupancy of SMARCA4) (Figure 6G).

ATAC-seq experiments revealed striking changes in the accessibility landscape across all 4 cell lines, with losses in accessibility at over 30,000 sites genome-wide upon FHD-286 treatment (Figures 6H, S6E, and S6F). Decreases in accessibility were exemplified over the gene loci of tuft cell lineage markers *AVIL*, *CHAT*, *GFI1B*, and *SOX9* at which we also identified near complete loss of POU2F3 binding coupled with reduced occupancy of H3K27Ac and RNA Pol II<sup>13,14</sup> (Figures 6I and S6G). Notably, these lost sites were largely TSS-distal implicating altered enhancer accessibility and top motifs significantly enriched were those corresponding to the POU2F3 TF family (Oct1, 2, 6, and 11) (Figures 6J and S6H). Integrating these accessibility findings with gene expression, we identified a collection of POU2F3 signature genes impacted via both chromatin accessibility and mRNA levels (Figure 6K). Taken together, these data show that mSWI/SNF ATPase inhibition uniformly impacts the accessibility over POU2F3 targets in POU2F3-positive SCLC, resulting in an attenuation of POU2F3 target chromatin accessibility and gene expression.

We next sought to define the genes selectively impacted by FHD-286-mediated ATPase inhibition relative to FHD-609-mediated BRD9 degradation in the non-NE cell lines exhibiting sensitivity to both agents. We identified gene sets concordantly up- and downregulated upon both FHD-609 and FHD-286 treatments in the NCI-H1048 and NCI-H211 cells, as well as genes and gene pathways that were only affected by FHD-286 (Figure S6I). In general, a greater number of genes were impacted by FHD-286, and genes impacted by both agents

were up- or downregulated with higher amplitude upon FHD-286 relative to FHD-609 (Figures 6L–6N). In addition, we identified significant changes in genes corresponding to differentiation, reduction in epithelial-mesenchymal transition (EMT), increased expression of P53 targets, increased senescence and reduction in metastasis signatures (Figure 6O). Further, expression of genes that were specifically downregulated by FHD-286 in non-NE cell lines was higher in the NE-like cell lines (COR-L311 and NCI-H526) that selectively responded to FHD-286 (and not FHD-609), demonstrating a gene level basis for the differential sensitivity (Figure 6P). These data demonstrate the chromatin and gene regulatory impacts of FHD-286-mediated mSWI/SNF inhibition across POU2F3-positive SCLC and define sets of genes that are similarly and disparately regulated by ncBAF complexes and the mSWI/SNF family at-large.

### mSWI/SNF pharmacologic disruption impacts POU2F3 and co-activators OCA-T1/2

Treatment of all POU2F3-positive SCLC cell lines with SMARCA4/2 inhibitors (FHD-286 and BRM014) and with BRD9 degraders (FHD-609 and VA-68-VQ71) resulted in marked attenuation of expression of the POU2F3 gene signature defined by Vakoc and colleagues<sup>13</sup> (Figures 7A–7C and S7A; Table S5). Of note, both treatments also dramatically attenuated signatures mediated by POU2F3 co-activators, OCA-T1 and OCA-T2<sup>13</sup> (Figures 7B, 7C, and S7B). Notably, treatment with FHD-286 resulted in reduction of accessibility over the *POU2F3*, *POU2AF3* (*COLCA2*), and *POU2AF2* (*C11ORF53*) loci (including promoters and distal enhancers) (Figure 7D). BRD9-marked ncBAF complexes were also reduced in occupancy across all three loci upon FHD-286 treatment. SMARCA4 and SS18 were substantially reduced over the *POU2F3* locus, but more modestly reduced at *POU2AF3/POU2AF2* promoters (and reduced more

### Figure 6. mSWI/SNF ATPase inhibition attenuates oncogenic SCLC gene regulatory networks

- (A) PCA analysis performed on RNA-seq experiments in DMSO control and FHD-286-treated conditions (100 nM for 72 h) across four POU2F3-positive SCLC cell lines.
- (B) GSEA analysis showing consistently and significantly downregulated pathways by FHD-286 across all four SCLC cell lines.
- (C) Volcano plots showing significantly downregulated (blue) and upregulated (red) genes in non-NE cell lines, NCI-H1048 and NCI-H211; and in NE-like cell lines, COR-L311 and NCI-H526 upon FHD-286 treatment.
- (D) Venn diagrams reflecting overlap between downregulated (top) and upregulated (bottom) genes impacted in non-NE and NE-like cell lines. Selected genes are labeled.
- (E) Venn diagram showing overlap between SMARCA4 ChIP-seq peaks in FHD-286 vs. DMSO control in NCI-H1048 cells.
- (F) HOMER motif analysis performed over lost SMARCA4 sites from (E).
- (G) Heatmaps depicting chromatin accessibility and SMARCA4, SS18, BRD9, POU2F3 ChIP-seq peak signal performed over merged SMARCA4 sites from (E); input shown as control.
- (H) Heatmaps depicting lost, retained, and gained ATAC-seq peaks upon FHD-286 treatment called across the merged set of ATAC-seq peaks in each SCLC cell line.
- (I) Representative tracks at the *AVIL* and *CHAT* loci showing ATAC-seq signal, and POU2F3, RBP1, H3K27Ac ChIP-seq in DMSO and FHD-286 conditions. Bar graphs showing gene expression in DMSO and FHD-286 conditions are shown (right).
- (J) HOMER motif analyses performed across all 4 POU2F3-positive lines showing top motifs in lost, retained, and gained accessibility sites.
- (K) Integrative RNA-seq and ATAC-seq analyses in DMSO- and FHD-286-treated conditions in NCI-H1048 and NCI-H211 lines shown as Z-scored (RNA) and LFC (ATAC) heatmaps.
- (L) Heatmap reflecting concordant changes in gene expression in NCI-H1048 and NCI-H211 cell lines upon FHD-286 or FHD-609 treatment.
- (M) Venn diagrams depicting concordant differentially expressed genes following treatment with FHD-286 or FHD-609.
- (N) Dot plot showing concordant and differential gene expression Hallmark GSEA pathways impacted by FHD-286 and FHD-609.
- (O) Dot plot showing concordant and differential GSEA C2 pathways impacted by FHD-286 and FHD-609 across cell lines indicated.
- (P) Box and whisker plot depicting average expression of genes specifically impacted by FHD-286 (FHD-286-only genes) in non-NE cell lines across all four POU2F3<sup>+</sup> SCLCs. The centerlines indicate the median. The box limits indicate the 25% and 75% percentiles. The whiskers indicate 25% percentile – 1.5 \* IQR and 75% percentile + 1.5 \* IQR. IQR = 75% percentile value – 25% percentile value. *p* value is indicated and was calculated using a pairwise t test between NE and non-NE cell lines. \*\*\**p* < 0.001. See also Figure S6.

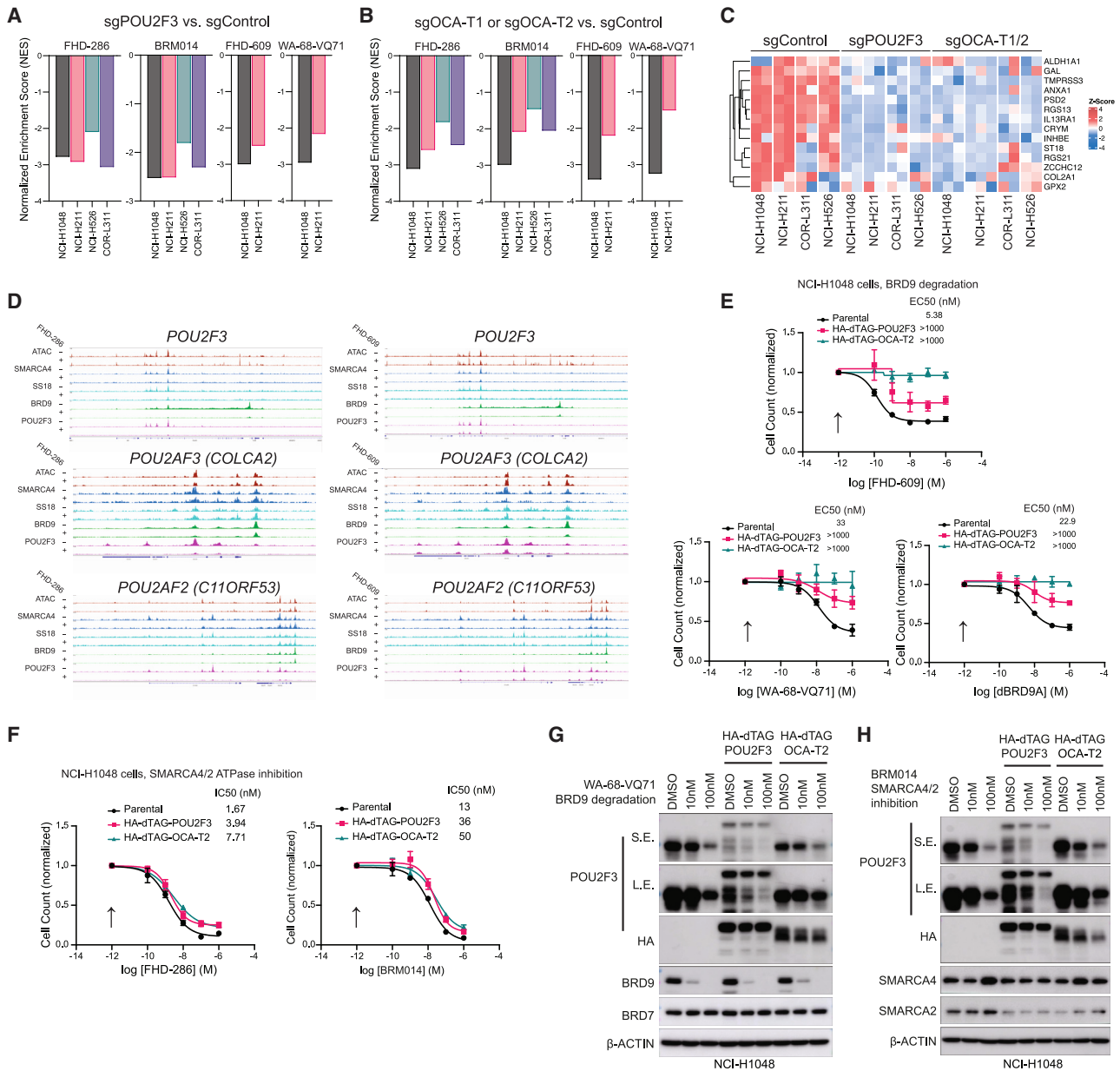


**Figure 7. mSWI/SNF pharmacologic disruption impacts expression and activity of POU2F3 TF and co-activators OCA-T1/2**

(A and B) Normalized enrichment score (NES) of downregulated genes after treatment with SMARCA4/2 inhibitors (FHD-286 or BRM014) or BRD9 degraders (FHD-609 or WA-68-VQ71) at 100 nM for 72 h comparing sgPOU2F3 vs. sgControl (A) or sgOCA-T1 (for NCI-H211, NCI-H526, COR-L311) or sgOCA-T2 (for NCI-H1048) vs. sgControl (B) from Wu et al., 2022.<sup>13</sup>  $n = 3$  biological replicates for FHD-286, FHD-609.  $n = 2$  biological replicates for BRM014, WA-68-VQ71.

(C) Heatmap depicting expression (Z score [RPKM values]) of sgPOU2F3 or OCA-T1/2 signature genes from (A) and (B).

(D) Chromatin targeting (ChIP-seq for SMARCA4 [BRG1], SS18, BRD9, POU2F3) and accessibility regulation (ATAC-seq) at the *POU2F3*, *POU2AF3*, and *POU2AF2* loci in NCI-H1048 cells treated with (left) FHD-286 (100 nM) or (right) FHD-609 (100 nM) for 72 h.

(E) Dose response assays of NCI-H1048 Cas9 cells expressing exogenous sgRNA-resistant HA-dTAG-POU2F3 or HA-dTAG-OCA-T2 with knockout of endogenous POU2F3 or OCA-T2, respectively, or parental NCI-H1048 cells treated with BRD9 degraders (FHD-609, WA-68-VQ71, and dBRD9a) for 6 days.

(F) Cells in (E) treated with FHD-286 (left) or BRM014 (right) for 6 days. For (E) and (F),  $n = 3$  biological replicates; cell counts are normalized to DMSO condition. Arrows indicate DMSO-treated sample used for normalization. Error bars represent mean  $\pm$  SEM.

(G and H) Immunoblot analyses on cells from (E) and (F) treated with WA-68-VQ71 or BRM014 for 72 h. See also Figure S7 and Table S5.

prominently at the *POU2AF2* enhancer) (Figure 7D). With FHD-609 treatment, SMARCA4 and SS18 occupancy was reduced at all three loci, along with near complete disappearance of BRD9

(consistent with its degradation); however, POU2F3 occupancy was only modestly reduced (Figure 7D). Notably, treatment with FHD-609 did not alter chromatin accessibility, and at some

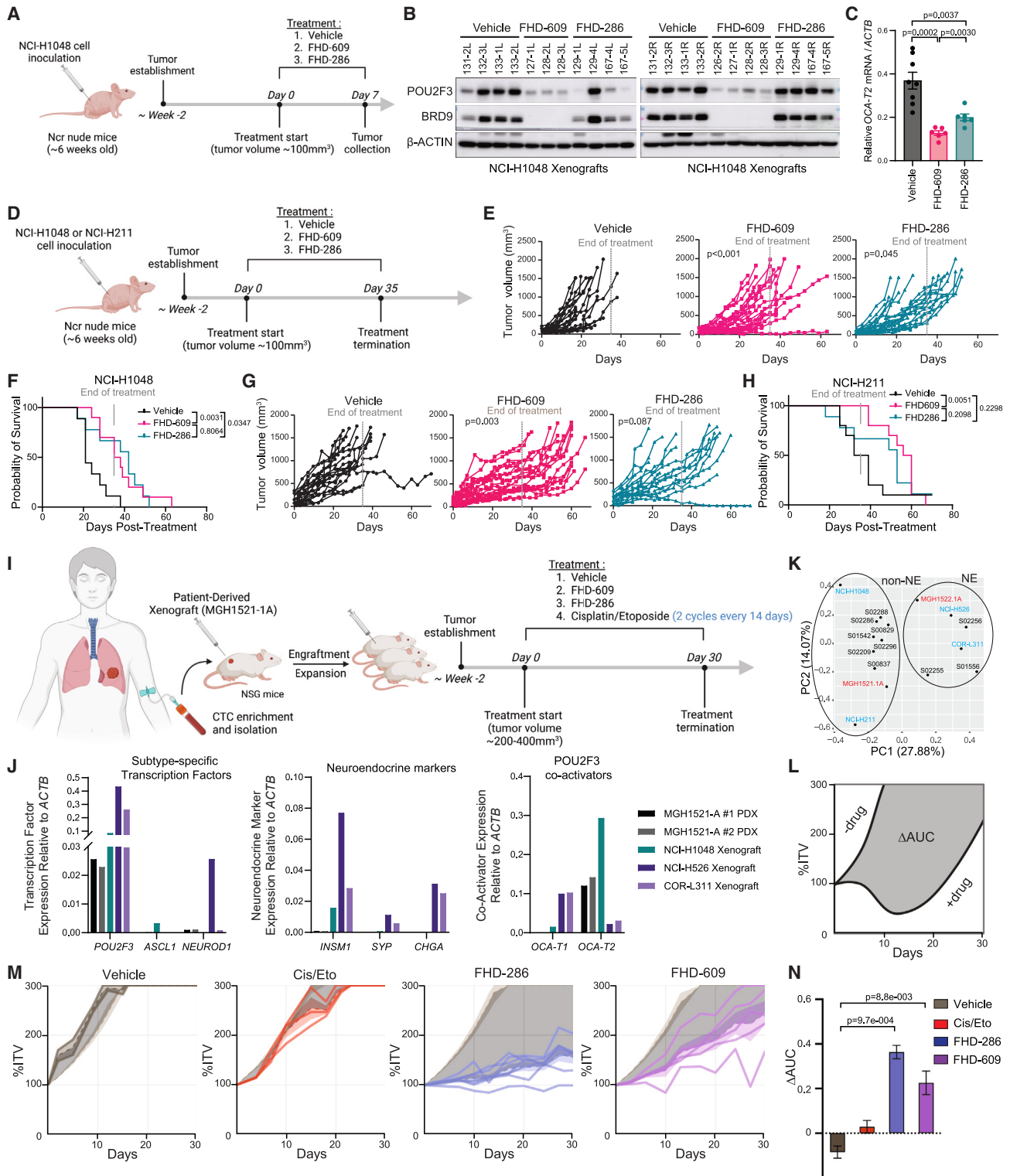


**Figure 8. The BRD9 degrader FHD-609 or SMARCA4/2 inhibitor FHD-286 slows tumor growth and increases survival in POU2F3 SCLC xenograft models**

(A) Schema for the pharmacodynamic (PD) study in NCI-H1048 xenografts where NCr-nude mice harboring subcutaneous xenografts were treated daily for 7 days with 0.5 mg/kg FHD-609 by intraperitoneal injection (IP), 1.5 mg/kg FHD-286 by oral gavage (PO), or vehicle (HP-β-CD).  $n = 4$  independent mice each with 1–2 tumors per mouse.

(legend continued on next page)

loci increased accessibility (Figure 7D). To determine whether POU2F3 interacts with mSWI/SNF complexes, we performed immunoprecipitation experiments in all four POU2F3-positive lines, which showed weak binding particularly to the SMARCD1 core component of ncBAF (and all mSWI/SNF complexes) (Figure S7D). These data suggest a programmatic attenuation in the POU2F3-mediated gene signature that is achieved by pharmacologic inhibition of mSWI/SNF complexes.

We next sought to define the specific contributions of POU2F3 and co-activator (OCA-T2) expression on the antiproliferative effects caused by SMARCA4/2 ATPase inhibition or BRD9 degradation. We used CRISPR-Cas9 to knockout endogenous POU2F3 or OCA-T2<sup>13</sup> and expressed exogenous, sgRNA-resistant POU2F3 or OCA-T2 under a short EF1alpha ubiquitous promoter (EFS) fused to a dTAG<sup>48,49</sup> in NCI-H1048 cells (Figures S7E–S7G). Dose response assays with three independent BRD9 degraders (FHD-609, WA-68-VQ71, and dBRD9A) and two SMARCA4/2 ATPase inhibitors (FHD-286 and BRM014) were then performed (Figures 7E and 7F). Strikingly, exogenous POU2F3 or OCA-T2 expression rendered SCLC cells uniformly resistant to all BRD9 degraders, while not affecting the efficacy of either SMARCA4/2 inhibitor (Figures 7E and 7F) suggesting that pan mSWI/SNF ATPase inhibition results in effects beyond POU2F3/OCA-T2. Consistent with this, immunoblot analysis revealed that BRD9 degradation decreased endogenous POU2F3 without altering exogenous POU2F3 or OCA-T2 protein levels (Figure 7G). In contrast, and consistent with proliferation experiments, SMARCA4/2 inhibition (BRM014) decreased both endogenous POU2F3 and exogenous POU2F3 and OCA-T2 (Figure 7H). Together, these results demonstrate that POU2F3 loss itself is responsible for the anti-proliferative effects observed with BRD9 degraders but that POU2F3 levels more modestly contribute to the anti-proliferative impact achieved with SMARCA2/4 inhibition.

### Clinical-grade pharmacologic disruption of mSWI/SNF complexes slows tumor growth and improves survival of POU2F3-positive SCLCs

We then treated POU2F3-positive SCLC xenograft models (NCI-H1048 and NCI-H211) with either FHD-609 (BRD9 degrader) or FHD-286 (SMARCA4/2 inhibitor), both of which have entered phase I clinical trials for other indications. Pharmacodynamic (PD) experiments in NCI-H1048 xenografts demonstrated that FHD-609 completely degrades BRD9 protein with a corresponding decrease of OCA-T2 in all tumors (Figures 8A–8C). FHD-286 also decreased OCA-T2 expression (Figure 8C). We next performed efficacy studies in NCI-H1048 and NCI-H211 xenografts treated with FHD-609, FHD-286, or vehicle for 35 days continuously and then monitored off treatment for survival (Figure 8D). Importantly, both FHD-609 and FHD-286 significantly inhibited NCI-H1048 tumor growth and increased survival relative to mice treated with vehicle (Figures 8E, 8F, S8A, and S8B). Similar results were observed in the NCI-H211 model (Figures 8G, 8H, S8C, and S8D). Tumor growth and survival impacts occurred absent changes in body weight, suggesting that FHD-609 and FHD-286 were both well tolerated (Figures S8E and S8F).

Among the SCLC subtypes, POU2F3-positive SCLCs are the least responsive to front-line chemotherapy.<sup>8,50</sup> We therefore tested whether the addition of FHD-286 or FHD-609 is additive when combined with cisplatin/etoposide front-line chemotherapy. Efficacy studies in NCI-H1048 xenografts were performed in mice treated with cisplatin/etoposide, FHD-286, FHD-609, FHD-286 + cisplatin/etoposide, FHD-609 + cisplatin/etoposide, or vehicle (Figures S8G and S8H). Cisplatin/etoposide did slow tumor growth, but did not cause frank tumor regressions (Figure S8J). Consistent with our aforementioned experiments, FHD-286 and FHD-609 also suppressed tumor growth (Figure S8J). Contrast estimates from linear mixed effects models to compare the observed combination treatment

(B and C) Immunoblot analysis (B) and RT-qPCR (C) of the tumors from (A). For (B),  $n = 8$  vehicle-treated tumors,  $n = 7$  FHD-609-treated tumors, and  $n = 7$  FHD-286-treated tumors. For (C),  $n = 8$  vehicle-treated tumors,  $n = 6$  FHD-609-treated tumors, and  $n = 6$  FHD-286-treated tumors.  $p$  values were calculated using a 2-tailed unpaired  $t$  test. Error bars represent mean  $\pm$  SEM.

(D) Schema for the *in vivo* efficacy experiments in NCI-H1048 and NCI-H211 xenografts where Ncr-nude mice harboring NCI-H1048 or NCI-H211 subcutaneous xenografts were treated daily (QD) for 35 days with FHD-609 (0.5 mg/kg IP), FHD-286 (1.5 mg/kg PO), or vehicle (HP- $\beta$ -CD), and then monitored for survival.

(E and F) Spider plots of individual NCI-H1048 xenograft tumors (E) and Kaplan-Meier survival of mice (F) treated with vehicle (black), FHD-609 (pink), or FHD-286 (blue). For (E) and (F),  $n = 18$  tumors from 9 independent mice (vehicle),  $n = 20$  tumors from 10 independent mice (FHD-609), and  $n = 18$  tumors from 9 independent mice (FHD-286).

(G and H) Spider plots of individual NCI-H211 xenograft tumors (G) and Kaplan-Meier survival of mice (H) treated with vehicle (black), FHD-609 (pink), or FHD-286 (blue). For (G) and (H);  $n = 17$  tumors from 10 independent mice (vehicle),  $n = 18$  tumors from 10 independent mice (FHD-609), and  $n = 15$  tumors from 9 independent mice (FHD-286). For the spider plots in (E) and (G),  $p$  values are indicated and were obtained from a linear mixed-effects model calculating the difference between the change in tumor volume (TV) relative to vehicle (see Methods) while tumors were on treatment (until D35). For Kaplan-Meier survival curves (F) and (H),  $p$  values are indicated and calculated using Gehan-Breslow-Wilcoxon test.

(I) Schema for the *in vivo* efficacy experiments in POU2F3-positive PDX MGH1521-1A in NSG mice.

(J) RT-qPCR of subcutaneous xenograft tumors for POU2F3, ASCL1, NEUROD1, OCA-T1, OCA-T2, INSM1, SYP, and CHGA.

(K) PCA of gene expression from RNA-seq data of 2 POU2F3-expressing PDX models (non-NE [MGH1521-1A] or NE-like [MGH1522-1A]) shown in red and non-NE and NE-like POU2F3-expressing SCLC primary tumors<sup>4</sup> (in black) and cell lines (in blue).

(L) Schema for the PDX response using  $\Delta$ AUC for the efficacy experiments in (M) and (N). Dark gray shading = difference in area under treated and untreated average TV curves ( $\Delta$ AUC).

(M) TV curves of individual MGH1521-1A PDX tumors treated with vehicle, cisplatin/etoposide (5 mg/kg cisplatin on day 1 and 8 mg/kg etoposide on days 1, 2, and 3 every 14 days), FHD-286 (1.5 mg/kg PO QD), or FHD-609 (0.5 mg/kg IP QD). Solid color lines = TV curves for treated xenografts starting from initial tumor volume (ITV) of 200–400 mm<sup>3</sup>. Dashed color lines + color shading = average TV-curves  $\pm$ 95% confidence interval (CI). Tan dashed lines + shading = untreated TV curves  $\pm$ 95% CI from model growth coefficients calculated from 17 mice with MGH1521-1A xenografts. Dark gray shading = difference in area under treated and untreated average TV curves ( $\Delta$ AUC).

(N) Quantitation of  $\Delta$ AUC of tumors in (M) with adjusted  $p$  values from Dunnett's T3 test comparing vehicle ( $n = 2$ ) with FHD-286 ( $n = 7$ ), FHD-609 ( $n = 5$ ), or Cis/Eto ( $n = 3$ , adj.  $p > 0.1$ ). Figures 8A–8D, and 8I were created with BioRender. See also Figure S8 and Table S6.

effects with the expected individual treatment effects (see [STAR methods](#)) showed that FHD-286 + cisplatin/etoposide or FHD-609 + cisplatin/etoposide were indeed additive and not antagonistic ([Figures S8K and S8L](#)). Moreover, FHD-286 + cisplatin/etoposide or FHD-609 + cisplatin/etoposide were well tolerated ([Figure S8I](#)). These data support use of FHD-286 or FHD-609 in combination with front-line chemotherapy.

Lastly, we tested efficacy of FHD-286 or FHD-609 in a POU2F3-positive patient-derived xenograft (PDX) MGH1521-1A<sup>51</sup> ([Figure 8I](#)). MGH1521-1A was derived from circulating tumor cells at initial diagnosis from a chemotherapy-naïve patient with extensive-stage SCLC. Consistent with poor outcomes in POU2F3-positive human SCLCs,<sup>8,50</sup> this patient was refractory to first-line chemotherapy and passed away 63 days after diagnosis, shortly after beginning a second cycle of carboplatin/etoposide ([Table S6](#)).<sup>51</sup> RT-qPCR showed that MGH1521-1A was most consistent with a pure non-NE POU2F3-positive SCLC with OCA-T2 co-activator expression ([Figure 8J](#)). Consistent with this, PCA showed that MGH1521-1A clustered closely with pure non-NE POU2F3-positive SCLC cell lines and primary tumors ([Figure 8K](#)).<sup>4,51</sup> In line with our prior study,<sup>51</sup> the MGH1521-1A POU2F3 PDX model was insensitive to cisplatin/etoposide chemotherapy ([Figures 8L–8N](#)). Strikingly, treatment with FHD-286 resulted in near-complete growth inhibition for 30 days, long after expected tumor progression upon standard platinum-doublet chemotherapy ([Figures 8L–8N](#)). Similar efficacy was observed for FHD-609, echoing the responses of POU2F3-positive non-NE models NCI-H211 and NCI-H1048 to both SMARCA4/2 ATPase inhibition and ncBAF disruption. Both FHD-286 and FHD-609 were well tolerated without causing overt toxicity or weight loss ([Table S6](#)). Together, these *in vivo* results nominate clinical-grade mSWI/SNF-targeting small molecules as potential therapeutic agents in the treatment of the POU2F3 subtype of SCLC.

## DISCUSSION

SCLC is a highly lethal form of lung cancer that still lacks effective targeted therapies.<sup>2</sup> Studies over the past several years have demonstrated that SCLC relies on lineage-specific TFs including ASCL1, NEUROD1, and POU2F3, all of which currently remain undruggable targets.<sup>3,11–16,40</sup> Here, through a positive selection genome-wide CRISPR-Cas9 screen for POU2F3 regulators coupled with proliferation-based dependency screens,<sup>40</sup> we identified pivotal roles for mSWI/SNF chromatin remodeling complexes in the regulation of POU2F3 TF expression and maintenance of POU2F3-mediated oncogenic gene expression and proliferation. We find that all POU2F3-positive SCLCs are highly sensitive to the clinical-grade pan-mSWI/SNF inhibitor, FHD-286, including those that retain expression of canonical neuroendocrine markers. Surprisingly, we identify a subset of POU2F3-positive SCLCs that are purely non-NE lines and are hypersensitive to ncBAF inhibition with clinical-grade BRD9 degraders. Together, our results suggest that pan-mSWI/SNF ATPase inhibition merits further evaluation as a therapeutic strategy for the broad class of POU2F3-positive SCLCs, while BRD9 degradation should be tested in POU2F3-positive SCLCs that are purely non-NE.

At the molecular level, we find that mSWI/SNF inhibition causes substantial loss of chromatin accessibility at POU2F3 target genes, including POU2F3 itself, implicating its autoregulation. Globally, SMARCA4/2 ATPase inhibition via FHD-286 results in a substantially greater global “reset” of the chromatin landscape, with the majority of affected sites reduced in accessibility, as expected, relative to FHD-609-mediated degradation of the ncBAF-specific subunit, BRD9. In non-NE SCLC cellular models, FHD-609-mediated ncBAF disruption led to more selective accessibility losses over POU2F3 target sites, while pan-mSWI/SNF inhibition reduced accessibility over these sites and those corresponding to other TFs. These data highlight the SCLC addiction to the POU2F3 TF-driven signature enabled by mSWI/SNF-mediated chromatin accessibility generation; secondary gene pathways are supported broadly by mSWI/SNF family chromatin remodelers, rather than the ncBAF subcomplex in isolation. These findings are further supported by rescue experiments where exogenous POU2F3 or OCA-T2 expression selectively rescues the cellular proliferation defects caused by BRD9 degraders but not those caused by pan-mSWI/SNF complex ATPase inhibition.

Human POU2F3-positive SCLC has historically been considered to be a purely non-neuroendocrine subtype of SCLC.<sup>3,7</sup> Here we found that all POU2F3-positive human SCLC cell lines were selectively hypersensitive to inhibition of mSWI/SNF, but only some cell lines were hypersensitive to disruption of ncBAF through BRD9 degradation. ncBAF complexes are the most recently characterized and do not appear to have homologous complexes in yeast, suggesting that they as an entity are the most evolutionarily recent. Interestingly, they are known to target CTCF sites genome-wide, implicating potential roles in genome organization and topology that are distinct from cBAF and PBAF remodeler complexes.<sup>39,45</sup> Through unbiased analyses, we found gene signatures associated with ncBAF sensitivity, which included differences in neuroendocrine marker expression. Specifically, POU2F3-positive cell lines that retained expression of neuroendocrine markers were inherently resistant to BRD9 degradation, while cell lines with complete absence of neuroendocrine markers were hypersensitive to BRD9 degradation. Human POU2F3-positive SCLC primary tumors<sup>4,47</sup> also showed that POU2F3-positive human SCLC segregates into mostly pure non-neuroendocrine tumors with fewer POU2F3-positive tumors retaining some neuroendocrine marker expression. Our findings suggest potential therapeutic relevance for further subclassification of the POU2F3 subtype into pure non-neuroendocrine tumors or tumors that retain neuroendocrine marker expression, especially relevant given that BRD9 degraders and SMARCA4/2 inhibitors are currently being tested in clinical trials for other cancer indications. Deciding on the appropriate therapeutic approach in non-neuroendocrine POU2F3-positive SCLCs will require additional efforts to evaluate the toxicities of each therapeutic strategy to maximize therapeutic window. Moreover, given the limited number of POU2F3-positive human SCLCs available with transcriptome sequencing, future studies will also require a larger number of samples to further refine mechanistic findings in the setting of transcriptional heterogeneity.

Our data show anti-tumor efficacy of a clinical-grade BRD9 degrader (FHD-609) or clinical-grade SMARCA4/2 ATPase

inhibitor (FHD-286) in POU2F3-positive SCLC xenograft models and a POU2F3-positive PDX model without overt toxicity. Our findings are in agreement with two recent studies showing efficacy of a SMARCA4/2 ATPase inhibitor BRM014<sup>52</sup> or SMARCA4/2 ATPase degrader AU-24118<sup>53</sup> in POU2F3-positive cell line xenografts. POU2F3-positive SCLC is the least responsive SCLC subtype to front-line chemotherapy<sup>8,50</sup> suggesting that new upfront therapeutic approaches for the POU2F3-subtype are needed either in lieu of chemotherapy or in combination with chemotherapy. We observed meaningful anti-tumor activity with BRD9 degraders and SMARCA4/2 inhibitors, but we did not observe striking tumor regressions suggesting that combination strategies should be considered. Our combination efficacy experiments of SMARCA4/2 inhibitors or BRD9 degraders with front-line cisplatin/etoposide revealed additive efficacy suggesting a combination strategy to improve responses. Interestingly, ncBAF complexes have been implicated in homologous recombination and DNA repair.<sup>54</sup> BRD9 inactivation has been shown to sensitize ovarian cancer cells to PARP inhibition,<sup>54</sup> which is particularly relevant given that POU2F3-positive SCLC cell lines are highly sensitive to PARP inhibitors.<sup>8</sup>

Finally, recent evidence suggests that SCLC subtypes could be regulated by distinct epigenetic modifiers. Our data suggest that only the POU2F3 subtype is highly dependent on mSWI/SNF. Previous studies found that some SCLC cell lines of the ASCL1 subtype are highly dependent on the histone demethylase LSD1, where LSD1 is dispensable in other SCLC subtypes.<sup>55,56</sup> As such, the identification of the biochemical and chromatin regulatory interplay between lineage-specific TFs and each distinct chromatin regulatory entity is likely to yield improved understanding regarding SCLC pathogenesis and uncover additional therapeutic vulnerabilities associated with each SCLC subtype.

### Limitations of the study

While we identify and validate that mSWI/SNF complexes represent top-ranked, chemically targetable vulnerabilities in POU2F3-positive SCLC, the number of available cell lines and *in vivo* models remains limited. Further, the programmatic changes in oncogenic gene expression upon mSWI/SNF disruption described here very likely exhibit increased variability in human tumors. Finally, our positive selection genome-wide CRISPR-Cas9 screen for POU2F3 regulators was restricted to the NCI-H1048 cell line and involved the use of POU2F3-DCK\* as a suicide gene that kills cells treated with BVdU.<sup>37</sup> Therefore, this approach is designed for positive rather than negative selection, leading us to focus on genes that when inactivated caused BVdU resistance. Moreover, we cannot rule out the possibility of false negatives given that this was a positive selection assay in a cell line with a POU2F3 dependency, and hence there could be counter negative selection for POU2F3 loss and its positive regulators.

### STAR★METHODS

Detailed methods are provided in the online version of this paper and include the following:

- KEY RESOURCES TABLE
- RESOURCE AVAILABILITY

- Lead contact
- Materials availability
- Data and code availability
- EXPERIMENTAL MODEL AND STUDY PARTICIPANT DETAILS
  - Mouse models
  - Cell lines
- METHOD DETAILS
  - Homology-directed repair using the Alt-R CRISPR-Cas9 system and homology-directed repair donor
  - Flow cytometry
  - BVdU sensitivity and rescue experiments
  - BVdU-positive selection CRISPR-Cas9 screen
  - sgRNA cloning to make lentiviruses
  - Lentivirus production
  - Lentiviral infection
  - Pharmacological inhibitors
  - Cell proliferation assays
  - Dose response assays
  - Crystal violet staining
  - Immunoblotting
  - RNA-sequencing
  - ATAC-sequencing
  - ChIP-sequencing studies
  - ChIP-Rx
  - Co-immunoprecipitation experiments
  - Exogenous POU2F3 and OCA-T2 rescue experiments
  - Reverse-transcriptase quantitative PCR (RT-qPCR)
  - Small cell lung cancers cell line xenografts and treatment studies
  - Patient-derived xenografts and treatment studies
  - Data analysis
  - ATAC-seq analysis
  - ChIP-seq analysis
  - RNA sequencing data analysis
  - Correlation analyses of validated enriched screen hits with POU2F3 dependency or POU2F3 expression
  - SMARCD1, BRD9 and BAF complexes gene effect calculations
- QUANTIFICATION AND STATISTICAL ANALYSES

### SUPPLEMENTAL INFORMATION

Supplemental information can be found online at <https://doi.org/10.1016/j.ccell.2024.06.012>.

### ACKNOWLEDGMENTS

We thank members of the Oser and Kadoch labs for their critical feedback. We are grateful to the DFCI Molecular Biology Core Facility including Zach Herbert and Maura Berkeley. This work was supported by a Novartis DDTRP grant (M.G.O.), NCI R37CA269990 (M.G.O.), a Damon Runyon Clinical Investigator Award (CI-101-19, M.G.O.), the Kaplan Family Foundation (M.G.O.), the Mark Foundation for Cancer Research Emerging Leader Award (C.K.), the Howard Hughes Medical Institute (C.K.), the Cancer Prevention & Research Institute of Texas (CPRIT) RR20007 (B.J.D.), and the NIH K08CA237832 (B.J.D.). K.S. was supported by the National Science Foundation Graduate Research Fellowship Program.

### AUTHOR CONTRIBUTIONS

L.D. and K.S.: conceptualization, methodology, validation, formal analysis, investigation, data curation, writing - original draft, visualization, project administration. S.P.C.: methodology, investigation, resources, data curation, visualization, supervision, project administration. X.L.: investigation, methodology, validation, formal analysis, data curation. A.W.Y., Y.L., X.Q., R.L., and S.S.: formal analysis, data curation, visualization, methodology. X.S.W.: methodology, investigation. S. H. and V.D.C.: investigation and data curation. Q.L. and J.Q.: chemical synthesis and resources. C.R.V. and H.W.L.: resources, supervision. H.M.H. and E.M.: formal analysis. Y.L. and J.G.D.: methodology. T.D.D.S., W.C.F., T.Z., T.A., and M.J.N.: resources. B.J.D.: methodology,

data curation, supervision, resources. C.K. and M.G.O: conceptualization, methodology, investigation, resources, data curation, writing - original draft, visualization, supervision, project administration, funding acquisition.

#### DECLARATION OF INTERESTS

M.G.O. reports grants from Eli Lilly, Takeda, Novartis, BMS, and Circle Pharma. C.K. is the Scientific Founder, Scientific Advisor to the Board of Directors, Scientific Advisory Board member, shareholder, and consultant for Foghorn Therapeutics, Inc. (Cambridge, MA), serves on the Scientific Advisory Boards of Nereid Therapeutics, Nested Therapeutics, and and Fibrogen, Inc. and is a consultant for Cell Signaling Technologies, Accent Therapeutics, and Google Ventures. C.K. is also a member of the *Molecular Cell* and *Cell Chemical Biology* Editorial Boards. B.J.D. has received consulting fees from AstraZeneca, Sonata Therapeutics and Dialectic Therapeutics. C.R.V. has received consulting fees from Flare Therapeutics, Roivant Sciences and C4 Therapeutics; has served on the advisory boards of KSQ Therapeutics, Syros Pharmaceuticals and Treeline Biosciences; has received research funding from Boehringer-Ingelheim and Treeline Biosciences; and owns stock in Treeline Biosciences.

Received: December 19, 2023

Revised: April 22, 2024

Accepted: June 21, 2024

Published: July 18, 2024

#### REFERENCES

1. Kalemkerian, G.P., Akerley, W., Bogner, P., Borghaei, H., Chow, L.Q., Downey, R.J., Gandhi, L., Ganti, A.K.P., Govindan, R., Grecula, J.C., et al. (2013). Small cell lung cancer. *J. Natl. Compr. Canc. Netw.* *11*, 78–98.
2. Rudin, C.M., Brambilla, E., Faivre-Finn, C., and Sage, J. (2021). Small-cell lung cancer. *Nat. Rev. Dis. Primers* *7*, 3. <https://doi.org/10.1038/s41572-020-00235-0>.
3. Rudin, C.M., Poirier, J.T., Byers, L.A., Dive, C., Dowlati, A., George, J., Heymach, J.V., Johnson, J.E., Lehman, J.M., MacPherson, D., et al. (2019). Molecular subtypes of small cell lung cancer: a synthesis of human and mouse model data. *Nat. Rev. Cancer* *19*, 289–297. <https://doi.org/10.1038/s41568-019-0133-9>.
4. George, J., Lim, J.S., Jang, S.J., Cun, Y., Ozretić, L., Kong, G., Leenders, F., Lu, X., Fernández-Cuesta, L., Bosco, G., et al. (2015). Comprehensive genomic profiles of small cell lung cancer. *Nature* *524*, 47–53. <https://doi.org/10.1038/nature14664>.
5. Peifer, M., Fernández-Cuesta, L., Sos, M.L., George, J., Seidel, D., Kasper, L.H., Plenker, D., Leenders, F., Sun, R., Zander, T., et al. (2012). Integrative genome analyses identify key somatic driver mutations of small-cell lung cancer. *Nat. Genet.* *44*, 1104–1110. <https://doi.org/10.1038/ng.2396>.
6. Rudin, C.M., Durinck, S., Stawiski, E.W., Poirier, J.T., Modrusan, Z., Shames, D.S., Bergbower, E.A., Guan, Y., Shin, J., Guillory, J., et al. (2012). Comprehensive genomic analysis identifies SOX2 as a frequently amplified gene in small-cell lung cancer. *Nat. Genet.* *44*, 1111–1116. <https://doi.org/10.1038/ng.2405>.
7. Baine, M.K., Febres-Aldana, C.A., Chang, J.C., Jungbluth, A.A., Sethi, S., Antonescu, C.R., Travis, W.D., Hsieh, M.S., Roh, M.S., Homer, R.J., et al. (2022). POU2F3 in SCLC: Clinicopathologic and Genomic Analysis With a Focus on Its Diagnostic Utility in Neuroendocrine-Low SCLC. *J. Thorac. Oncol.* *17*, 1109–1121. <https://doi.org/10.1016/j.jtho.2022.06.004>.
8. Gay, C.M., Stewart, C.A., Park, E.M., Diao, L., Groves, S.M., Heeke, S., Nabet, B.Y., Fujimoto, J., Solis, L.M., Lu, W., et al. (2021). Patterns of transcription factor programs and immune pathway activation define four major subtypes of SCLC with distinct therapeutic vulnerabilities. *Cancer Cell* *39*, 346–360.e7. <https://doi.org/10.1016/j.ccell.2020.12.014>.
9. Owonikoko, T.K., Dwivedi, B., Chen, Z., Zhang, C., Barwick, B., Ernani, V., Zhang, G., Gilbert-Ross, M., Carlisle, J., Khuri, F.R., et al. (2021). YAP1 Expression in SCLC Defines a Distinct Subtype With T-cell-Inflamed Phenotype. *J. Thorac. Oncol.* *16*, 464–476. <https://doi.org/10.1016/j.jtho.2020.11.006>.
10. Mahadevan, N.R., Knelson, E.H., Wolff, J.O., Vajdi, A., Saigi, M., Campisi, M., Hong, D., Thai, T.C., Piel, B., Han, S., et al. (2021). Intrinsic immunogenicity of small cell lung carcinoma revealed by its cellular plasticity. *Cancer Discov.* *11*, 1952–1969. <https://doi.org/10.1158/2159-8290.CD-20-0913>.
11. Borromeo, M.D., Savage, T.K., Kollipara, R.K., He, M., Augustyn, A., Osborne, J.K., Girard, L., Minna, J.D., Gazdar, A.F., Cobb, M.H., and Johnson, J.E. (2016). ASCL1 and NEUROD1 Reveal Heterogeneity in Pulmonary Neuroendocrine Tumors and Regulate Distinct Genetic Programs. *Cell Rep.* *16*, 1259–1272. <https://doi.org/10.1016/j.celrep.2016.06.081>.
12. Augustyn, A., Borromeo, M., Wang, T., Fujimoto, J., Shao, C., Dospoy, P.D., Lee, V., Tan, C., Sullivan, J.P., Larsen, J.E., et al. (2014). ASCL1 is a lineage oncogene providing therapeutic targets for high-grade neuroendocrine lung cancers. *Proc. Natl. Acad. Sci. USA* *111*, 14788–14793. <https://doi.org/10.1073/pnas.1410419111>.
13. Wu, X.S., He, X.Y., Ipsaro, J.J., Huang, Y.H., Preall, J.B., Ng, D., Shue, Y.T., Sage, J., Egeblad, M., Joshua-Tor, L., and Vakoc, C.R. (2022). OCA-T1 and OCA-T2 are coactivators of POU2F3 in the tuft cell lineage. *Nature* *607*, 169–175. <https://doi.org/10.1038/s41586-022-04842-7>.
14. Huang, Y.H., Klingbeil, O., He, X.Y., Wu, X.S., Arun, G., Lu, B., Somerville, T.D.D., Milazzo, J.P., Wilkinson, J.E., Demerdash, O.E., et al. (2018). POU2F3 is a master regulator of a tuft cell-like variant of small cell lung cancer. *Genes Dev.* *32*, 915–928. <https://doi.org/10.1101/gad.314815.118>.
15. Szczepanski, A.P., Tsuboyama, N., Watanabe, J., Hashizume, R., Zhao, Z., and Wang, L. (2022). POU2AF2/C11orf53 functions as a coactivator of POU2F3 by maintaining chromatin accessibility and enhancer activity. *Sci. Adv.* *8*, eabq2403. <https://doi.org/10.1126/sciadv.abq2403>.
16. Zhou, C., Huang, H., Wang, Y., Sendinc, E., and Shi, Y. (2022). Selective regulation of tuft cell-like small cell lung cancer by novel transcriptional co-activators C11orf53 and COLCA2. *Cell Discov.* *8*, 112. <https://doi.org/10.1038/s41421-022-00470-7>.
17. Tantin, D. (2013). Oct transcription factors in development and stem cells: insights and mechanisms. *Development* *140*, 2857–2866. <https://doi.org/10.1242/dev.095927>.
18. Chan, J.M., Zaidi, S., Love, J.R., Zhao, J.L., Setty, M., Wadosky, K.M., Gopalan, A., Choo, Z.N., Persad, S., Choi, J., et al. (2022). Lineage plasticity in prostate cancer depends on JAK/STAT inflammatory signaling. *Science* *377*, 1180–1191. <https://doi.org/10.1126/science.abn0478>.
19. Schneider, C., O’Leary, C.E., and Locksley, R.M. (2019). Regulation of immune responses by tuft cells. *Nat. Rev. Immunol.* *19*, 584–593. <https://doi.org/10.1038/s41577-019-0176-x>.
20. Gerbe, F., Sidot, E., Smyth, D.J., Ohmoto, M., Matsumoto, I., Dardalhon, V., Cesses, P., Garnier, L., Pouzolles, M., Brulin, B., et al. (2016). Intestinal epithelial tuft cells initiate type 2 mucosal immunity to helminth parasites. *Nature* *529*, 226–230. <https://doi.org/10.1038/nature16527>.
21. Yamaguchi, T., Yamashita, J., Ohmoto, M., Aoudé, I., Ogura, T., Luo, W., Bachmanov, A.A., Lin, W., Matsumoto, I., and Hirota, J. (2014). Skn-1a/Pou2f3 is required for the generation of Trpm5-expressing microvillous cells in the mouse main olfactory epithelium. *BMC Neurosci.* *15*, 13. <https://doi.org/10.1186/1471-2202-15-13>.
22. Matsumoto, I., Ohmoto, M., Narukawa, M., Yoshihara, Y., and Abe, K. (2011). Skn-1a (Pou2f3) specifies taste receptor cell lineage. *Nat. Neurosci.* *14*, 685–687. <https://doi.org/10.1038/nn.2820>.
23. Andersen, B., Weinberg, W.C., Rennekampff, O., McEvelly, R.J., Bermingham, J.R., Jr., Hooshmand, F., Vasilyev, V., Hansbrough, J.F., Pittelkow, M.R., Yuspa, S.H., and Rosenfeld, M.G. (1997). Functions of the POU domain genes Skn-1a/i and Tst-1/Oct-6/SCIP in epidermal differentiation. *Genes Dev.* *11*, 1873–1884. <https://doi.org/10.1101/gad.11.14.1873>.
24. Centore, R.C., Sandoval, G.J., Soares, L.M.M., Kadoch, C., and Chan, H.M. (2020). Mammalian SWI/SNF Chromatin Remodeling Complexes: Emerging Mechanisms and Therapeutic Strategies. *Trends Genet.* *36*, 936–950. <https://doi.org/10.1016/j.tig.2020.07.011>.

25. St Pierre, R., and Kadoch, C. (2017). Mammalian SWI/SNF complexes in cancer: emerging therapeutic opportunities. *Curr. Opin. Genet. Dev.* *42*, 56–67. <https://doi.org/10.1016/j.gde.2017.02.004>.
26. Xiao, L., Parolia, A., Qiao, Y., Bawa, P., Eyunni, S., Mannan, R., Carson, S.E., Chang, Y., Wang, X., Zhang, Y., et al. (2022). Targeting SWI/SNF ATPases in enhancer-addicted prostate cancer. *Nature* *601*, 434–439. <https://doi.org/10.1038/s41586-021-04246-z>.
27. Sun, A., Tawfik, O., Gayed, B., Thrasher, J.B., Hoestje, S., Li, C., and Li, B. (2007). Aberrant expression of SWI/SNF catalytic subunits BRG1/BRM is associated with tumor development and increased invasiveness in prostate cancers. *Prostate* *67*, 203–213. <https://doi.org/10.1002/pros.20521>.
28. Roy, N., Malik, S., Villanueva, K.E., Urano, A., Lu, X., Von Figura, G., Seeley, E.S., Dawson, D.W., Collisson, E.A., and Hebrok, M. (2015). Brg1 promotes both tumor-suppressive and oncogenic activities at distinct stages of pancreatic cancer formation. *Genes Dev.* *29*, 658–671. <https://doi.org/10.1101/gad.256628.114>.
29. Kim, S.Y., Shen, Q., Son, K., Kim, H.S., Yang, H.D., Na, M.J., Shin, E., Yu, S., Kang, K., You, J.S., et al. (2021). SMARCA4 oncogenic potential via IRAK1 enhancer to activate Gankyrin and AKR1B10 in liver cancer. *Oncogene* *40*, 4652–4662. <https://doi.org/10.1038/s41388-021-01875-6>.
30. Jubierre, L., Soriano, A., Planells-Ferrer, L., Paris-Coderch, L., Tenbaum, S.P., Romero, O.A., Moubarak, R.S., Almazán-Moga, A., Molist, C., Roma, J., et al. (2016). BRG1/SMARCA4 is essential for neuroblastoma cell viability through modulation of cell death and survival pathways. *Oncogene* *35*, 5179–5190. <https://doi.org/10.1038/onc.2016.50>.
31. Guerrero-Martinez, J.A., and Reyes, J.C. (2018). High expression of SMARCA4 or SMARCA2 is frequently associated with an opposite prognosis in cancer. *Sci. Rep.* *8*, 2043. <https://doi.org/10.1038/s41598-018-20217-3>.
32. Buscarlet, M., Krasteva, V., Ho, L., Simon, C., Hébert, J., Wilhelm, B., Crabtree, G.R., Sauvageau, G., Thibault, P., and Lessard, J.A. (2014). Essential role of BRG, the ATPase subunit of BAF chromatin remodeling complexes, in leukemia maintenance. *Blood* *123*, 1720–1728. <https://doi.org/10.1182/blood-2013-02-483495>.
33. Cyrt, J., Augspach, A., De Filippo, M.R., Prandi, D., Thienger, P., Benelli, M., Cooley, V., Bareja, R., Wilkes, D., Chae, S.S., et al. (2020). Role of specialized composition of SWI/SNF complexes in prostate cancer lineage plasticity. *Nat. Commun.* *11*, 5549. <https://doi.org/10.1038/s41467-020-19328-1>.
34. Kofink, C., Trainor, N., Mair, B., Wöhrle, S., Wurm, M., Mischerikow, N., Roy, M.J., Bader, G., Greb, P., Garavel, G., et al. (2022). A selective and orally bioavailable VHL-recruiting PROTAC achieves SMARCA2 degradation in vivo. *Nat. Commun.* *13*, 5969. <https://doi.org/10.1038/s41467-022-33430-6>.
35. Farnaby, W., Koegl, M., Roy, M.J., Whitworth, C., Diers, E., Trainor, N., Zollman, D., Steurer, S., Karolyi-Oezguer, J., Riedmueller, C., et al. (2019). BAF complex vulnerabilities in cancer demonstrated via structure-based PROTAC design. *Nat. Chem. Biol.* *15*, 672–680. <https://doi.org/10.1038/s41589-019-0294-6>.
36. Papillon, J.P.N., Nakajima, K., Adair, C.D., Hempel, J., Jouk, A.O., Karki, R.G., Mathieu, S., Möbitz, H., Ntaganda, R., Smith, T., et al. (2018). Discovery of Orally Active Inhibitors of Brahma Homolog (BRM)/SMARCA2 ATPase Activity for the Treatment of Brahma Related Gene 1 (BRG1)/SMARCA4-Mutant Cancers. *J. Med. Chem.* *61*, 10155–10172. <https://doi.org/10.1021/acs.jmedchem.8b01318>.
37. Koduri, V., Duplaquet, L., Lampson, B.L., Wang, A.C., Sabet, A.H., Ishoey, M., Paulk, J., Teng, M., Harris, I.S., Endress, J.E., et al. (2021). Targeting oncoproteins with a positive selection assay for protein degraders. *Sci. Adv.* *7*, eabd6263. <https://doi.org/10.1126/sciadv.abd6263>.
38. Sanson, K.R., Hanna, R.E., Hegde, M., Donovan, K.F., Strand, C., Sullender, M.E., Vaimberg, E.W., Goodale, A., Root, D.E., Piccioni, F., and Doench, J.G. (2018). Optimized libraries for CRISPR-Cas9 genetic screens with multiple modalities. *Nat. Commun.* *9*, 5416. <https://doi.org/10.1038/s41467-018-07901-8>.
39. Michel, B.C., D'Avino, A.R., Cassel, S.H., Mashtalir, N., McKenzie, Z.M., McBride, M.J., Valencia, A.M., Zhou, Q., Bocker, M., Soares, L.M.M., et al. (2018). A non-canonical SWI/SNF complex is a synthetic lethal target in cancers driven by BAF complex perturbation. *Nat. Cell Biol.* *20*, 1410–1420. <https://doi.org/10.1038/s41556-018-0221-1>.
40. Tsherniak, A., Vazquez, F., Montgomery, P.G., Weir, B.A., Kryukov, G., Cowley, G.S., Gill, S., Harrington, W.F., Pantel, S., Krill-Burger, J.M., et al. (2017). Defining a Cancer Dependency Map. *Cell* *170*, 564–576.e16. <https://doi.org/10.1016/j.cell.2017.06.010>.
41. Mashtalir, N., D'Avino, A.R., Michel, B.C., Luo, J., Pan, J., Otto, J.E., Zullo, H.J., McKenzie, Z.M., Kubiak, R.L., St Pierre, R., et al. (2018). Modular Organization and Assembly of SWI/SNF Family Chromatin Remodeling Complexes. *Cell* *175*, 1272–1288.e20. <https://doi.org/10.1016/j.cell.2018.09.032>.
42. Netherton, M.R. (2023). Discovery of FHD-609: A Potent and Selective Heterobifunctional Degradator of BRD9. *Drug Discovery Chemistry Meeting*.
43. Hentemann, M. (2022). Pharmacological profile and anti-tumor properties of FHD-286: A novel BAF inhibitor for the treatment of transcription factor-driven cancers.
44. Jagani, Z., Chenail, G., Xiang, K., Bushold, G., Bhang, H.E.C., Li, A., Elliott, G., Zhu, J., Vattay, A., Gilbert, T., et al. (2019). In-Depth Characterization and Validation in BRG1-Mutant Lung Cancers Define Novel Catalytic Inhibitors of SWI/SNF Chromatin Remodeling. Preprint at bioRxiv. <https://doi.org/10.1101/812628>.
45. St Pierre, R., Collings, C.K., Samé Guerra, D.D., Widmer, C.J., Bolonduro, O., Mashtalir, N., Sankar, A., Liang, Y., Bi, W.L., Gerkes, E.H., et al. (2022). SMARCE1 deficiency generates a targetable mSWI/SNF dependency in clear cell meningioma. *Nat. Genet.* *54*, 861–873. <https://doi.org/10.1038/s41588-022-01077-0>.
46. Balanis, N.G., Sheu, K.M., Esedebe, F.N., Patel, S.J., Smith, B.A., Park, J.W., Alhani, S., Gomperts, B.N., Huang, J., Witte, O.N., and Graeber, T.G. (2019). Pan-cancer Convergence to a Small-Cell Neuroendocrine Phenotype that Shares Susceptibilities with Hematological Malignancies. *Cancer Cell* *36*, 17–34.e7. <https://doi.org/10.1016/j.ccell.2019.06.005>.
47. Liu, Q., Zhang, J., Guo, C., Wang, M., Wang, C., Yan, Y., Sun, L., Wang, D., Zhang, L., Yu, H., et al. (2024). Proteogenomic characterization of small cell lung cancer identifies biological insights and subtype-specific therapeutic strategies. *Cell* *187*, 184–203.e28. <https://doi.org/10.1016/j.cell.2023.12.004>.
48. Nabet, B., Ferguson, F.M., Seong, B.K.A., Kuljanin, M., Leggett, A.L., Mohardt, M.L., Robichaud, A., Conway, A.S., Buckley, D.L., Mancias, J.D., et al. (2020). Rapid and direct control of target protein levels with VHL-recruiting dTAG molecules. *Nat. Commun.* *11*, 4687. <https://doi.org/10.1038/s41467-020-18377-w>.
49. Nabet, B., Roberts, J.M., Buckley, D.L., Paulk, J., Dastjerdi, S., Yang, A., Leggett, A.L., Erb, M.A., Lawlor, M.A., Souza, A., et al. (2018). The dTAG system for immediate and target-specific protein degradation. *Nat. Chem. Biol.* *14*, 431–441. <https://doi.org/10.1038/s41589-018-0021-8>.
50. Nabet, B.Y., Hamidi, H., Lee, M.C., Banchereau, R., Morris, S., Adler, L., Gayevskiy, V., Elhossiny, A.M., Srivastava, M.K., Patil, N.S., et al. (2024). Immune heterogeneity in small-cell lung cancer and vulnerability to immune checkpoint blockade. *Cancer Cell* *42*, 429–443.e4. <https://doi.org/10.1016/j.ccell.2024.01.010>.
51. Pal Choudhuri, S., Girard, L., Lim, J.Y.S., Wise, J.F., Freitas, B., Yang, D., Wong, E., Hamilton, S., Chien, V.D., Kim, Y.J., et al. (2024). Acquired Cross-resistance in Small Cell Lung Cancer due to Extrachromosomal DNA Amplification of MYC paralogs. *Cancer Discov.* *14*, 804–827. <https://doi.org/10.1158/2159-8290.CD-23-0656>.
52. Szczepanski, A., Tsuboyama, N., Lyu, H., Wang, P., Beytullahoglu, O., Zhang, T., Singer, B.D., Yue, F., Zhao, Z., and Wang, L. (2024). A SWI/SNF-dependent transcriptional regulation mediated by POU2AF2/C11orf53 at enhancer. *Nat. Commun.* *15*, 2067. <https://doi.org/10.1038/s41467-024-46492-5>.

53. He, T., Xiao, L., Qiao, Y., Klingbeil, O., Young, E., Wu, X.S., Mannan, R., Mahapatra, S., Eyunni, S., Ching-Yi Tien, J., et al. (2024). Targeting the mSWI/SNF Complex in POU2F-POU2AF Transcription Factor-Driven Malignancies. *Cancer Cell*, 42. <https://doi.org/10.1016/j.ccell.2024.06.006>.
54. Zhou, Q., Huang, J., Zhang, C., Zhao, F., Kim, W., Tu, X., Zhang, Y., Nowshheen, S., Zhu, Q., Deng, M., et al. (2020). The bromodomain containing protein BRD-9 orchestrates RAD51-RAD54 complex formation and regulates homologous recombination-mediated repair. *Nat. Commun.* 11, 2639. <https://doi.org/10.1038/s41467-020-16443-x>.
55. Augert, A., Eastwood, E., Ibrahim, A.H., Wu, N., Grunblatt, E., Basom, R., Liggitt, D., Eaton, K.D., Martins, R., Poirier, J.T., et al. (2019). Targeting NOTCH activation in small cell lung cancer through LSD1 inhibition. *Sci. Signal.* 12, eaau2922. <https://doi.org/10.1126/scisignal.aau2922>.
56. Chen, H.Y., Durmaz, Y.T., Li, Y., Sabet, A.H., Vajdi, A., Denize, T., Walton, E., Laimon, Y.N., Doench, J.G., Mahadevan, N.R., et al. (2022). Regulation of neuroendocrine plasticity by the RNA-binding protein ZFP36L1. *Nat. Commun.* 13, 4998. <https://doi.org/10.1038/s41467-022-31998-7>.
57. Danecek, P., Bonfield, J.K., Liddle, J., Marshall, J., Ohan, V., Pollard, M.O., Whitwham, A., Keane, T., McCarthy, S.A., Davies, R.M., and Li, H. (2021). Twelve years of SAMtools and BCFtools. *GigaScience* 10, giab008. <https://doi.org/10.1093/gigascience/giab008>.
58. Zhang, Y., Liu, T., Meyer, C.A., Eeckhoute, J., Johnson, D.S., Bernstein, B.E., Nusbaum, C., Myers, R.M., Brown, M., Li, W., and Liu, X.S. (2008). Model-based analysis of ChIP-Seq (MACS). *Genome Biol.* 9, R137. <https://doi.org/10.1186/gb-2008-9-9-r137>.
59. Love, M.I., Huber, W., and Anders, S. (2014). Moderated estimation of fold change and dispersion for RNA-seq data with DESeq2. *Genome Biol.* 15, 550. <https://doi.org/10.1186/s13059-014-0550-8>.
60. Gu, Z., Eils, R., and Schlesner, M. (2016). Complex heatmaps reveal patterns and correlations in multidimensional genomic data. *Bioinformatics* 32, 2847–2849. <https://doi.org/10.1093/bioinformatics/btw313>.
61. Orlando, D.A., Chen, M.W., Brown, V.E., Solanki, S., Choi, Y.J., Olson, E.R., Fritz, C.C., Bradner, J.E., and Guenther, M.G. (2014). Quantitative ChIP-Seq normalization reveals global modulation of the epigenome. *Cell Rep.* 9, 1163–1170. <https://doi.org/10.1016/j.celrep.2014.10.018>.
62. Dobin, A., Davis, C.A., Schlesinger, F., Drenkow, J., Zaleski, C., Jha, S., Batut, P., Chaisson, M., and Gingeras, T.R. (2013). STAR: ultrafast universal RNA-seq aligner. *Bioinformatics* 29, 15–21. <https://doi.org/10.1093/bioinformatics/bts635>.
63. <https://broadinstitute.github.io/picard/>.
64. Langmead, B., and Salzberg, S.L. (2012). Fast gapped-read alignment with Bowtie 2. *Nat. Methods* 9, 357–359. <https://doi.org/10.1038/nmeth.1923>.
65. Quinlan, A.R., and Hall, I.M. (2010). BEDTools: a flexible suite of utilities for comparing genomic features. *Bioinformatics* 26, 841–842. <https://doi.org/10.1093/bioinformatics/btq033>.
66. Bonfield, J.K., Marshall, J., Danecek, P., Li, H., Ohan, V., Whitwham, A., Keane, T., and Davies, R.M. (2021). HTSlib: C library for reading/writing high-throughput sequencing data. *GigaScience* 10, giab007. <https://doi.org/10.1093/gigascience/giab007>.
67. Larsson, J., and Gustafsson, P. (2018). A Case Study in Fitting Area-Proportional Euler Diagrams with Ellipses Using eulerr. In *Proceedings of International Workshop on Set Visualization and Reasoning 2116*, 84–91. <https://doi.org/10.32614/CRAN.package.eulerr>.
68. Heinz, S., Benner, C., Spann, N., Bertolino, E., Lin, Y.C., Laslo, P., Cheng, J.X., Murre, C., Singh, H., and Glass, C.K. (2010). Simple combinations of lineage-determining transcription factors prime cis-regulatory elements required for macrophage and B cell identities. *Mol. Cell* 38, 576–589. <https://doi.org/10.1016/j.molcel.2010.05.004>.
69. Ramirez, F., Ryan, D.P., Gruning, B., Bhardwaj, V., Kilpert, F., Richter, A.S., Heyne, S., Dundar, F., and Manke, T. (2016). deepTools2: a next generation web server for deep-sequencing data analysis. *Nucleic Acids Res.* 44, W160–W165. <https://doi.org/10.1093/nar/gkw257>.
70. Thorvaldsdottir, H., Robinson, J.T., and Mesirov, J.P. (2013). Integrative Genomics Viewer (IGV): high-performance genomics data visualization and exploration. *Brief Bioinform.* 14, 178–192. <https://doi.org/10.1093/bib/bbs017>.
71. Bolstad, B. (2024). preprocessCore: A collection of pre-processing functions. R package version 1.66.0. <https://doi.org/10.18129/B9.bioc.preprocessCore>.
72. Wickham, H. (2016). *ggplot2: Elegant Graphics for Data Analysis* (Springer International Publishing).
73. Wu, T., Hu, E., Xu, S., Chen, M., Guo, P., Dai, Z., Feng, T., Zhou, L., Tang, W., Zhan, L., et al. (2021). clusterProfiler 4.0: A universal enrichment tool for interpreting omics data. *Innovation* 2, 100141. <https://doi.org/10.1016/j.xinn.2021.100141>.

**STAR★METHODS**

**KEY RESOURCES TABLE**

REAGENT or RESOURCE	SOURCE	IDENTIFIER
<b>Antibodies</b>		
Rabbit Anti-POU2F3	Cell Signaling Technology	Cat# 92579, RRID: AB_3096173
Rabbit Anti-ASCL1	Abcam	Cat# ab211327, RRID: AB_2924270
Rabbit Anti-NEUROD1(EPR4008)	Abcam	Cat# ab109224, RRID: AB_10861489
rabbit anti-DCK	Abcam	Cat# ab151966, RRID: AB_3096174
Rabbit anti-BRD9 (E9R2I)	Cell Signaling Technology	Cat# 58906, RRID: AB_3096175
Rabbit Anti-BRD7 (D9K2T)	Cell Signaling Technology	Cat# 15125, RRID:AB_2798719
Rabbit Anti-SMARCD1 (E7W9W)	Cell Signaling Technology	Cat# 35070, RRID: AB_3096176
Rabbit Anti-BICRA (E6I3A)	Cell Signaling Technology	Cat# 45441, RRID: AB_3095741
Rabbit Anti-BICRAL (GLTSCR1L)	Thermo Fisher Scientific	Cat# PA5-56126, RRID: AB_2642051
Rabbit Anti-OCA-T1	Cell Signaling Technology	Cat# 20217, RRID: AB_3096178
Rabbit Anti-SMARCA2 (BRM) (D9E8B)	Cell Signaling Technology	Cat# 11966, RRID: AB_2797783
Rabbit Anti-SMARCA4 (BRG1) (D1Q7F)	Cell Signaling Technology	Cat# 49360, RRID: AB_2728743
Rabbit Anti-HA (C29F4)	Cell Signaling Technology	Cat# 3724 (also 3724S), RRID: AB_1549585
Mouse Anti-HA.11 (16B12)	BioLegend	Cat# 901501 (also 901502, 901503, 901533), RRID: AB_2565006
Rabbit Anti-GSPT1	Abcam	Cat# ab49878, RRID: AB_2115507
Rabbit Anti-ACTL6B (E5X8C)	Cell Signaling Technology	Cat# 46787, RRID: AB_3096179
mouse $\alpha$ -INSM1	Santa Cruz	Cat# sc-377428, RRID: AB_2848191
Rabbit Anti-Synaptophysin (YE269)	Abcam	Cat# ab32127, RRID: AB_2286949
Rabbit Anti-Cleaved Caspase3 (Asp175) (5A1E)	Cell Signaling Technology	Cat# 9664 (also 9664P), RRID: AB_2070042
Mouse Anti- $\beta$ -actin	Sigma-Aldrich	Cat# A3854, RRID: AB_262011
Mouse Anti-Vinculin	Sigma-Aldrich	Cat# V9131, RRID: AB_477629
Peroxidase Goat Anti-Mouse	Jackson ImmunoResearch Labs	Cat# 115-035-003, RRID: AB_10015289
Peroxidase Goat anti-Rabbit	Jackson ImmunoResearch Labs	Cat# 111-035-003, RRID: AB_2313567
Rabbit Anti-POU2F3 (E5N2D)	Cell Signaling Technology	Cat# 36135, RRID: AB_2924784
mouse anti-Rpb1 (4H8)	Cell Signaling Technology	Cat# 2629, RRID: AB_2167468
Rabbit Anti-H3K27Ac (D5E4)	Cell Signaling Technology	Cat# 8173, RRID: AB_10949503
Recombinant Anti-BRG1	Abcam	Cat# ab110641, RRID: AB_10861578
Rabbit Anti-ARID1A (D2A8U)	Cell Signaling Technology	Cat#12354, RRID: AB_2637010
Rabbit Anti-BRD9 (E4Q3F)	Cell Signaling Technology	Cat#48306, RRID: AB_3095838
Rabbit Anti-SS18 (D6I4Z)	Cell Signaling Technology	Cat#21792, RRID: AB_2728667
Mouse Anti-ARID2 (GT7311)	Thermo Fisher Scientific	Cat# MA5-27862, RRID: AB_2735115
Mouse Anti-TBP (1TBP18)	Thermo Fisher Scientific	Cat# MA1-21516, RRID: AB_2199928
Rabbit Anti-SMARCC2 (D8O9V)	Cell Signaling Technology	Cat# 12760, RRID: AB_2798017
Goat Anti-BAF155 (SMARCC2)	Santa Cruz Biotechnology (SCBT)	Cat# sc-9746, RRID: AB_671099
Mouse Anti-BAF60a (SMARCD1) (23)	Santa Cruz Biotechnology (SCBT)	Cat# sc-135843, RRID: AB_2192137
Recombinant Anti-SMARCD2	Abcam	Cat# ab220164, RRID: AB_2904257
Mouse Anti-SMARCD2 (F-34)	Santa Cruz Biotechnology (SCBT)	Cat# sc-101162, RRID: AB_1129531
Mouse Anti-DPF2 (C9)	Santa Cruz Biotechnology (SCBT)	Cat# sc-514297, RRID: AB_3096211
Mouse Anti-PBRM1 (E6N2K)	Cell Signaling Technology	Cat# 81832, RRID: AB_3096212
Rabbit Anti-SMARCB1 (D8M1X)	Cell Signaling Technology	Cat# 91735, RRID: AB_2800172
Mouse Anti-ACTL6A	Santa Cruz Biotechnology (SCBT)	Cat# sc-137062, RRID: AB_2009388
Recombinant Rabbit IgG, monoclonal	Abcam	Cat#ab172730, RRID: AB_2687931
Mouse Anti-H2Av	Active Motif	Cat# 61751, RRID: AB_2793757

(Continued on next page)

**Continued**

REAGENT or RESOURCE	SOURCE	IDENTIFIER
IRDye 800CW Goat anti-Rabbit IgG Secondary Antibody	LI-COR Biosciences	Cat# 926-32211, RRID: AB_621843
IRDye 680RD Goat anti-Mouse IgG Secondary Antibody	LI-COR Biosciences	Cat#926-68070, RRID: AB_10956588
IRDye 680RD Donkey anti-Goat IgG Secondary Antibody	LI-COR Biosciences	Cat# 926-68074, RRID: AB_10956736
<b>Bacterial and virus strains</b>		
HB101	Promega	Cat#L2011
<b>Biological samples</b>		
Patient Derived Xenografts (PDXs)	Choudhuri et al., <i>Cancer Discov.</i> , 2024	phs003486.v1.p1
<b>Chemicals, peptides, and recombinant proteins</b>		
BVdU	Chem-Impex International Inc	Cat #27735, CAS # 69304-47-8
FHD-609	Jun Qi's Laboratory	N/A
FHD-286	Jun Qi's Laboratory	N/A
AU-15330	Jun Qi's Laboratory	N/A
dTAG-V1	Jun Qi's Laboratory	N/A
XHC-640	Novartis	N/A
WA-68-VQ71	Novartis	N/A
dBRD9A	Novartis	N/A
BRM014	Novartis	N/A
Cisplatin	Fresenius Kabi	Cat #100365
Etoposide	Hikma Pharmaceuticals USA	Cat #0143-9376-01
HP- $\beta$ -CD	Sigma Aldrich	Cat #778966
Puromycin	Gold BioTechnology	Cat #P-600-100, CAS #58-58-2
G418	Gold BioTechnology	Cat #G-418-10-SPO, CAS #108321-42-2
Blasticidin	Thermo Fisher Scientific	Cat #NC9016621
DMSO	Sigma Aldrich	Cat #D2650
TRIzol Reagent	Thermo Fisher Scientific	Cat #15596018
Tn5 transposase	Illumina	Cat #20034198
AMPure XP Beads	Beckman Coulter	Cat #A6388
Dynabeads M-280 Sheep Anti-Mouse IgG	Thermo Fisher Scientific	Cat #11201D
Dynabeads M-280 Sheep Anti-Rabbit IgG	Thermo Fisher Scientific	Cat #11204D
<b>Critical commercial assays</b>		
KOD HOT START DNA POLYMERASE	Fisher Scientific	Cat #710863
In-Fusion 5X HD Cloning Plus	Takara Bio	Cat #638909
NucleoSpin PCR Clean-up kit	Macherey-Nagel	Cat #740609.10
SF Cell Line Nucleofector™ Solution	Lonza	V4XC-2032
Genomic DNA maxi prep kit	Qiagen	Cat #51194
TURBO DNA-free™ Kit	Thermo Fisher Scientific	Cat #AM1907
BCA Protein Assay Kit	Thermo Fisher Scientific	Cat #23225
Protein Assay Dye Reagent	Bio-Rad Laboratories	Cat #5000006
Protease inhibitor cocktail (Complete)	Roche Applied Science	Cat #11836153001
phosphatase inhibitors (PhosSTOP)	Sigma Aldrich	Cat #04906837001
Immobilon detection reagents	Thermo Fisher Scientific	Cat #WBKLS0500
Supersignal West Pico	Thermo Fisher Scientific	Cat #PI34078
RNeasy mini kit	Qiagen	Cat #74106
NEBNext Ultra II Directional RNA Library Prep Kit for Illumina	New England Biolabs	Cat #E7760L
NEBNext Ultra II DNA Library Prep Kit for Illumina	New England Biolabs	Cat #E7645L

(Continued on next page)

**Continued**

REAGENT or RESOURCE	SOURCE	IDENTIFIER
MinElute Reaction Cleanup Kit	Qiagen	Cat #28204
Quick-RNA™ Miniprep kit	Zymo Research	Cat #1159U79
iScript Reverse Transcription Supermix	Bio-Rad Laboratories	Cat #1708841
LightCycler 480 Probes Master Kit	Roche	Cat #507203179
High Sensitivity D1000 ScreenTape	Agilent	Cat #5067-5584
High Sensitivity D1000 ScreenTape	Agilent	Cat #5067-5585
High Sensitivity D5000 ScreenTape	Agilent	Cat #5067-5592
High Sensitivity D5000 ScreenTape	Agilent	Cat #5067-5593

**Deposited data**

Human POU2F3 RNA-seq Analyses from publicly available RNA-seq Data	George et al. <sup>4</sup> ; Liu et al. <sup>47</sup>	GEO: GSE69091 GSA database: HRA003419
RNA-seq data of cells treated with BRM014 and WA-68-VQ71	GEO Database	GEO: GSE249258
RNA-seq data of cells treated with FHD-609 and FHD-286	GEO Database	GEO: GSE249362
ATAC- and ChIP-sequencing data	GEO Database	GEO: GSE249362

**Experimental Models: Cell Lines**

NCI-H1048	American Type Culture Collection (ATCC)	RRID: CVCL_1453
NCI-H526	American Type Culture Collection (ATCC)	RRID: CVCL_1569
NCI-H211	American Type Culture Collection (ATCC)	RRID: CVCL_1529
COR-L311	American Type Culture Collection (ATCC)	RRID: CVCL_2412
NCI-1092	American Type Culture Collection (ATCC)	RRID: CVCL_1454
NCI-H1836	American Type Culture Collection (ATCC)	RRID: CVCL_1498
LU135	American Type Culture Collection (ATCC)	RRID: CVCL_1389
293T	American Type Culture Collection (ATCC)	RRID: CVCL_0063
SCLC-22H	DSMZ	RRID: CVCL_2186
COR-L47	Sigma-Aldrich	RRID: CVCL_2415
NCI-H82	Dr. Kwok-kin Wong's laboratory (New York University)	RRID: CVCL_1591
Schneider 2	Thermo Fisher Scientific	Cat# R69007, RRID: CVCL_Z232

**Experimental Models: Organisms/Strains**

NCr nude mice (crtac:NCr-Foxn1nu)	Taconic Biosciences	RRID:IMSR_TAC:NCRNU
NSG mouse (NOD.Cg-Prkdcscid Il2rgtm1Wjl/SzJ)	Jackson Laboratory	RRID:BCBC_4142

**Oligonucleotides**

sgRNA oligos	IDT technologies	<a href="#">Table S7</a>
gBlocks™ Gene Fragments and primers for Knock-in	IDT technologies	<a href="#">Table S1</a>
crRNA oligo against POU2F3	IDT technologies	5'-AAACTTTTTGGTCTCAGTGG-3' (antisense)
TracrRNA	IDT technologies	IDT #1072533
Alt-R® S.p. Cas9 Nuclease V3	IDT technologies	IDT #1081059
Cas9-containing whole genome Brunello sgRNA library	Broad Institute	CP0043
POU2F3 Taqman probe	ThermoFisher Scientific	Hs00205009_m1
ASCL1 Taqman probe	ThermoFisher Scientific	Hs04187546_g1
NEUROD1 Taqman probe	ThermoFisher Scientific	Hs00159598_m1
OCA-T1 (C11ORF53) Taqman probe	ThermoFisher Scientific	Hs00736612_m1
OCA-T2 (COLCA2) Taqman probe	ThermoFisher Scientific	Hs00416978_m1
INSM1 Taqman probe	ThermoFisher Scientific	Hs00357871_s1
SYNAPTOPHYSIN Taqman probe	ThermoFisher Scientific	Hs00300531_m1

(Continued on next page)

**Continued**

REAGENT or RESOURCE	SOURCE	IDENTIFIER
CHROMOGRANIN-A Taqman probe	ThermoFisher Scientific	Hs00154441_m1
ACTIN-B Taqman probe	ThermoFisher Scientific	Hs01060665_g1
<b>Recombinant DNA</b>		
LentiCRISPRV2-Puro	Addgene	#98290
lentiCRISPRV2-Neo	Addgene	#98292
psPAX2	Addgene	#12260
pMD2.G	Addgene	#12259
pCRIS-PITCHv2-Puro-dTAG	Addgene	#91703
<b>Software and algorithms</b>		
FlowJo v10.5.3	FlowJo, LLC	<a href="https://www.flowjo.com/">https://www.flowjo.com/</a>
Graphpad Prism 10	Graphpad	<a href="https://www.graphpad.com/">https://www.graphpad.com/</a>
Gene Set Enrichment Analysis (GSEA)	Subramanian et al., 2005	<a href="http://www.broad.mit.edu/gsea/downloads.jsp">http://www.broad.mit.edu/gsea/downloads.jsp</a>
ImageJ Fiji	ImageJ	<a href="https://imagej.net/ij/">https://imagej.net/ij/</a>
APRON analysis (Pooled Screen Analysis Tool)	GPP Web Portal	<a href="https://portals.broadinstitute.org/gpp/public/">https://portals.broadinstitute.org/gpp/public/</a>
Hypergeometric analysis	GPP Web Portal	<a href="https://portals.broadinstitute.org/gpp/public/">https://portals.broadinstitute.org/gpp/public/</a>
STARS software	GPP Web Portal	<a href="https://portals.broadinstitute.org/gpp/public/">https://portals.broadinstitute.org/gpp/public/</a>
bcl2fastq v2.20.0.422	Illumina, Inc.	<a href="https://emea.support.illumina.com/sequencing/sequencing_software/bcl2fastq-conversion-software.html">https://emea.support.illumina.com/sequencing/sequencing_software/bcl2fastq-conversion-software.html</a>
STAR v2.5.2b	Alex Dobin	<a href="https://github.com/alexdobin/STAR">https://github.com/alexdobin/STAR</a>
Trimmomatic v0.36	Tony Bolger, Bjoern Usadel	<a href="https://github.com/usadellab/Trimmomatic">https://github.com/usadellab/Trimmomatic</a>
Bowtie2 v2.2.9	Langmead et al., 2019	<a href="https://github.com/BenLangmead/bowtie2">https://github.com/BenLangmead/bowtie2</a>
Picard v2.8.0	Broad Institute	<a href="https://github.com/broadinstitute/picard">https://github.com/broadinstitute/picard</a>
SAMtools v0.1.19	Danecek et al. <sup>57</sup>	<a href="https://github.com/samtools/samtools">https://github.com/samtools/samtools</a>
deepTools v3.5.3	Ramírez et al., 2016	<a href="https://github.com/deeptools/deepTools">https://github.com/deeptools/deepTools</a>
MACS3 v3.0.0b3	Zhang et al. <sup>58</sup>	<a href="https://github.com/mac3-project/MACS/">https://github.com/mac3-project/MACS/</a>
R v4.3.2	R Foundation	<a href="https://cran.r-project.org/bin/">https://cran.r-project.org/bin/</a>
R v4.3.3	R Foundation	<a href="https://cran.r-project.org/bin/">https://cran.r-project.org/bin/</a>
DESeq2 v1.40.2	Love et al. <sup>59</sup>	<a href="https://bioconductor.org/packages/release/bioc/html/DESeq2.html">https://bioconductor.org/packages/release/bioc/html/DESeq2.html</a>
ggplot2 v3.5.0	Hadley Wickham	<a href="https://cran.r-project.org/web/packages/ggplot2/index.html">https://cran.r-project.org/web/packages/ggplot2/index.html</a>
Eulerr v7.0.2	Johan Larsson	<a href="https://cran.r-project.org/web/packages/eulerr/index.html">https://cran.r-project.org/web/packages/eulerr/index.html</a>
ComplexHeatmap v2.16.0	Gu. et al. <sup>60</sup>	<a href="https://bioconductor.org/packages/release/bioc/html/ComplexHeatmap.html">https://bioconductor.org/packages/release/bioc/html/ComplexHeatmap.html</a>
msigdbr v7.5.1	Igor Dolgalev	<a href="https://cran.r-project.org/web/packages/msigdbr/index.html">https://cran.r-project.org/web/packages/msigdbr/index.html</a>
clusterProfiler v4.8.3	Yu et al., 2021	<a href="https://bioconductor.org/packages/release/bioc/html/clusterProfiler.html">https://bioconductor.org/packages/release/bioc/html/clusterProfiler.html</a>
limma package v3.58.1	Ritchie et al., 2015	<a href="https://bioconductor.org/packages/limma/">https://bioconductor.org/packages/limma/</a>

**RESOURCE AVAILABILITY**

**Lead contact**

Further information and requests for resources and reagents should be directed to and will be fulfilled by the lead contact, Matthew G. Oser ([matthew\\_oser@dfci.harvard.edu](mailto:matthew_oser@dfci.harvard.edu)).

### Materials availability

Materials and reagents can be requested from the [lead contact](#) upon reasonable request.

### Data and code availability

All sequencing raw and processed data (RNA-seq, ATAC-seq and ChIP-seq) have been deposited in the Gene Expression Omnibus (GEO) database and are publicly available under the series GEO: GSE249362, except RNA-seq data of cells treated with BRM014 and WA-68-VQ71 are in GEO under accession number GEO: GSE249258. Accession numbers are listed in the [key resources table](#).

This paper does not report original code.

Any additional information required to reanalyze the data reported in this paper is available from the [lead contact](#) upon request.

## EXPERIMENTAL MODEL AND STUDY PARTICIPANT DETAILS

### Mouse models

All mouse experiments complied with National Institutes of Health guidelines and were approved by Dana-Farber Cancer Institute Animal Care and Use Committee (DFCI, protocol 19–009) or with Institutional Animal Care and Use Committee–approved animal protocols in accordance with University of Texas Southwestern Medical Center institutional guidelines (protocol 2020–102859). For the cell line-xenograft study, Ncr nude mice (crtac:Ncr-Foxn1nu) were purchased from Taconic Biosciences (#NCRNU). Only females, 6 weeks old, were used. Housing conditions for mice at the DFCI Vi-varium include a 12 h/12 h day-night cycle where temperature is maintained at 72 Fahrenheit. For the PDX study, NSG mouse (NOD.Cg-Prkdc<sup>scid</sup> Il2rg<sup>tm1Wjl</sup>/SzJ) were purchased from Jackson Laboratory. Male and female, evenly divided, ~4–6 weeks old, were used. Housing conditions for mice at the University of Texas Southwestern Medical Center include a 12 h/12 h day-night cycle where temperature is maintained at 72 Fahrenheit.

### Cell lines

NCI-H1048 (09/2019), NCI-H526 (09/2019), NCI-H211 (01/2022), COR-L311 (01/2023), NCI-H1092(04/2018), NCI-H1836(07/2022), LU135 (07/2022), and 293T cells were obtained from American Type Culture Collection. SCLC-22H was purchased from DSMZ (01/2023). COR-L47 was obtained from Sigma (11/2018). NCI-H82 cells were a kind gift from Dr. Kwok-kin Wong's laboratory (New York University) and were obtained in 8/2014. NCI-H526, NCI-H211, COR-L311, COR-L47, NCI-H82 and LU135 cells were maintained in RPMI-1640 media with 10% FBS and P/S. NCI-H1048 cells were maintained in RPMI-1640 media with 10% FBS, P/S and ITS. NCI-H1092 and NCI-H1836 cells were maintained in DMEM/F12 media 5% FBS, P/S, and HITES. SCLC-22H and 293T were maintained in DMEM media with 10% FBS and P/S. S2 cells were grown in 25C with no CO2 supplementation. S2 cells were grown in Schneider's Drosophila medium (Gibco) supplemented with 10% FBS (Gibco) and 100 U/mL Penicillin-Streptomycin (Gibco). Early passage cell lines were tested for Mycoplasma (Lonza #LT07-218) and then were frozen using Bambanker's freezing media (Bulldog Bio). All experiments were performed with cell lines that were maintained in culture for <4 months at which time an early passage cell line was thawed.

## METHOD DETAILS

### Homology-directed repair using the Alt-R CRISPR-Cas9 system and homology-directed repair donor

#### Double-stranded homology-directed repair DNA template production

The DCK\*-P2A-GFP sequence was obtained performing two distinct PCR reactions using KOD HOT START DNA POLYMERASE (Fisher Scientific #710863) and the pLX304-DCK\*-IRES-GFP<sup>37</sup> vector as a template for overhang PCR that introduced linker1 and P2A onto the 5' and 3' ends of DCK\* or P2A and linker2 onto the 5' and 3' ends of GFP to obtain 2 PCR products: 1. linker1-DCK\*-P2A and 2. P2A-GFP-linker2 sequence. DCK\* is a variant of the deoxycytidine kinase with Ser74Glu, Arg104Met, and Asp133Ala substitutions. Then, an overlap PCR reaction was performed to obtain the linker1-DCK\*-P2A-GFP-linker2 (called DCK\*-P2A-GFP) sequence. In parallel, 2 double strand DNA sequences coding for the homology arms of *POU2F3* were designed and ordered from IDT as gBlocks Gene Fragments. Homology arm 1 is 300 nucleotides upstream of the endogenous stop codon of human *POU2F3* gene flanked by M13 pUC and Linker1 sequence (M13-HA1-linker1 called HA1). Homology arm 2 is 300 nucleotides downstream of the human *POU2F3* gene flanked by linker2 and M13 reverse sequence (Linker2-HA2-M13Rv called HA2). gBlocks (500 ng) were spin down before being resuspended at ~50 ng/μL in IDTE Buffer and incubated at 50°C for 15–20 min. An in-fusion cloning reaction was then performed using all 3 fragments above (HA1, HA2, and DCK\*-P2A-GFP) mixed with a purified inverse PCR product of the pDONR223 backbone that was made using M13 forward and M13 reverse primers. For the In-Fusion reaction, a 1:2 plasmid:insert (DCK\*-P2A-GFP/HA1/HA2) ratio was used [121.8 fmol (200 ng) of the pDONR223 PCR product mixed with 243 fmol of each dsDNA insert sequences] and then mixed with 2μL of In-Fusion 5X HD Cloning Plus (Takara Bio #638909). The reaction was incubated for 15 min at 37°C and stored at –20°C. The reaction mixture was then transformed at a ratio of 1:10 (reaction volume/volume competent cells) into HB101 competent cells (Promega #L2011). Spectinomycin-resistant colonies were screened by restriction digestion of miniprep DNA and subsequently validated by gel electrophoresis in a 0.8% agarose gel and by DNA sequencing. Finally, PCR reaction was performed on the newly synthesized vector to amplify the HA1-DCK\*-P2A-GFP-HA2 sequence corresponding to the homology-directed repair (HDR) DNA template and was purified using the NucleoSpin PCR Clean-up kit (Macherey-Nagel # 740609.10) according to the manufacturer's protocol. All DNA sequences used in the study are listed in [Table S1](#).

### **RNP production and nucleofection**

The RNP complex was produced by complexing a two-component gRNA to Cas9 according to the HDR protocol from IDT. Briefly, crRNA was designed using both the Broad Institute sgRNA designer tool (<http://portals.broadinstitute.org/gpp/public/analysis-tools/sgRNA-design>) and the IDT sgRNA designer tool ([https://www.idtdna.com/site/order/designtool/index/CRISPR\\_SEQUENCE](https://www.idtdna.com/site/order/designtool/index/CRISPR_SEQUENCE)) predicted to cut at a maximum of 6 nucleotides from the insertion site (before the endogenous stop codon of POU2F3 gene) and synthesized by IDT technologies. The following crRNA oligo predicted to cut 1 nucleotide before the insertion site was used: 5'-AAACTTTTTGGTCTCAGTGG-3' (antisense). To prepare gRNA complex, the designed crRNA and a TracrRNA (IDT# 1072533) were resuspended at 100  $\mu$ M in Nuclease-free duplex buffer, mixed 1:1 by volume and annealed by incubation at 95°C for 5 min. Then, the RNP complex was prepared by mixing gRNA complex with Alt-R S.p. Cas9 Nuclease V3 (IDT #1081059) at a ratio 2:3 by volume and incubated 20 min at room temperature. RNP was electroporated immediately after complexing. In parallel,  $1 \times 10^6$  NCI-H1048 cells were prepared, washed in sterile PBS, and resuspended in 20  $\mu$ L of SF Cell Line Nucleofector Solution with the supplement added (Lonza V4XC-2032). The cells and the RNP complex were carefully mixed and transferred to a well of the 16-well Nucleocuvette. Nucleofection was performed using CM-137 program on 4D-Nucleofector (Lonza). Cells were carefully resuspended with pre-warmed media, transferred into a 12 well plate and incubated at 37°C, 5% CO<sub>2</sub>. Cells were amplified for several days to allow FACS sorting for GFP-positive cells.

### **Validation of NCI-H1048 POU2F3-DCK\*-P2A-GFP knock-in cells**

NCI-H1048 cells nucleofected with the POU2F3-DCK\*-P2A-GFP dsDNA template were sorted twice by FACS for GFP expression to obtain a pure population expressing POU2F3-DCK\*-P2A-GFP fusion protein. Endogenous expression of POU2F3-DCK\* fusion protein and loss of the WT POU2F3 protein was confirmed by immunoblot analysis for POU2F3. Specificity of the knock-in for the POU2F3 locus was verified by blotting for DCK as the DCK immunoblot only showed 1 additional band, apart from endogenous DCK, at the expected molecular weight of the POU2F3-DCK\*-P2A-GFP fusion with an identical molecular weight also seen on the POU2F3 immunoblot. The functionality of POU2F3-DCK\* fusion was verified by BVdU dose response assays and rescue experiments with sgRNAs targeting DCK.

### **Flow cytometry**

NCI-H1048 parental and NCI-H1048 POU2F3-DCK\*-P2A-GFP cells were collected, washed twice in PBS, resuspended in FACS buffer (D-PBS containing 2% FBS), and transferred to flow cytometry tubes containing a 70  $\mu$ m filter and analyzed for GFP expression on an LSR Fortessa flow cytometer (Becton Dickinson, Franklin Lakes, NJ). Data were analyzed using FlowJo software.

### **BVdU sensitivity and rescue experiments**

NCI-H1048 parental and NCI-H1048 POU2F3-DCK\*-P2A-GFP cells were seeded into twelve-well plates at 50,000 cells per well in 0.5 mLs of complete media. Each well in the twelve-well dish received 0.5 mL of a stock solution of BVdU to achieve final BVdU concentrations of 1  $\mu$ M, 10  $\mu$ M, 100  $\mu$ M, 200  $\mu$ M and 500  $\mu$ M. A total of 0.5 mLs of media with DMSO was added to the sixth well as a control. Seven days later, the cells were collected and counted using a Vi-Cell XR cell counter. The same protocol was used for POU2F3 and DCK sgRNA rescue experiments using NCI-H1048 parental or NCI-H1048 POU2F3-DCK\*-P2A-GFP cells infected with a sgRNA targeting POU2F3, DCK or a non-targeting sgRNA and treated with BVdU (10  $\mu$ M) or DMSO for 7 days.

### **BVdU-positive selection CRISPR-Cas9 screen**

On day 0, NCI-H1048 POU2F3-DCK\*-P2A-GFP cells were counted.  $1.2 \times 10^8$  cells (which would yield a representation of  $\sim$ 500 cells/sgRNA) were pelleted and resuspended at  $2 \times 10^6$  cells/mL in complete media containing 50  $\mu$ L/mL of the Cas9-containing whole genome Brunello sgRNA library (CP0043)<sup>38</sup> (Purchased from the Broad Institute) lentivirus and 8  $\mu$ g/mL polybrene. The lentiviral titer was determined empirically in pilot experiments with a goal multiplicity of infection (MOI) of 0.3–0.5. CP0043 contains 77,441 sgRNAs targeting 4 sgRNAs per gene with 1000 non-targeting sgRNAs controls. The cells mixed with polybrene and lentivirus were then plated in 1 mL aliquots onto 12 well plates and centrifuged at 2000 rpm (931  $\times$  g) [Allegra X-15R Centrifuge (Beckman Coulter), rotor SX4750A] for 2 h at 30°C. In parallel,  $2 \times 10^6$  cells were also spin infected under the same conditions but without lentivirus as a control for puromycin selection (Mock).  $\sim$ 16 h later (day 1), the cells were collected, pooled, and centrifuged to remove the lentivirus and polybrene, and the cell pellet was resuspended in complete media at  $0.5 \times 10^6$  cells/mL and plated into ten 15 cm tissue culture treated plates at  $0.34 \times 10^6$  cells/mL or in 6 well plates for the control (Mock) cells. The cells were then cultured for 48 h at which time (day 3) the cells were counted and plated at  $0.4 \times 10^6$  cells/mL in 15 cm tissue culture treated plates with fresh media containing puromycin (0.25  $\mu$ g/mL) to select for puromycin-transduced cells. A parallel experiment was performed on day 3 to determine the MOI of the screen. To do this, the cells infected with the sgRNA library or mock-infected cells were plated at  $0.4 \times 10^6$  cells/mL in 6 well plates in the presence or absence of puromycin (0.25  $\mu$ g/mL). After 72 h (day 6), cells were counted using the Vi-Cell XR Cell Counter and the MOI was calculated using the following equation: (# of puromycin-resistant cells infected with the sgRNA library/# total cells surviving without puromycin after infection with the sgRNA library) – (# of puromycin-resistant mock-infected cells/# total mock-infected cells). The actual MOI was 0.56 for biological replicate 1 and 0.52 for biological replicate 2. On day 7, all puromycin-resistant cells were pooled, collected and counted. A total of  $2 \times 10^8$  cells were maintained to pursue the screen and were plated again at  $0.4 \times 10^6$  cells/mL with fresh media. On day 9, cells were pooled, counted and a total of  $4 \times 10^7$  cells for each condition (therefore maintaining at least 500 cells/guide) and were plated at  $0.05 \times 10^6$  cells/mL in 37 15 cm tissue culture plates with complete media containing BVdU (10  $\mu$ M) or at  $0.3 \times 10^6$  cells/mL in 6 15 cm tissue culture plates with complete media for

the untreated arm. At the same time, the remaining cells were collected and divided in aliquots of  $4 \times 10^7$  (again to maintain representation of at least 500 cells/guide), washed in PBS, and cell pellets were frozen for genomic DNA isolation for the initial timepoint prior to drug selection. On days 12 and 14, the cells from the untreated arm were pooled, counted, and a total of  $4 \times 10^7$  cells for each replicate were plated back at  $0.3 \times 10^6$  cells/mL into 6 15 cm tissue culture plates with fresh complete media. On day 16, 7 days after BVdU treatment, the screen was ended by collecting all remaining cells in both the BVdU and untreated conditions. As above, the remaining cells were divided in aliquots of  $4 \times 10^7$  cells, washed in PBS and cells pellets were frozen for genomic DNA isolation. The screen was performed in two biological replicates each with a separate infection.

Following completion of the screen, genomic DNA was isolated using the Qiagen Genomic DNA maxi prep kit (cat. # 51194) according to the manufacturer's protocol. Raw Illumina reads were normalized between samples using:  $\text{Log}_2[(\text{sgRNA reads}/\text{total reads for sample}) \times 1\text{e}6 + 1]$ . The initial common time point data (day 9) was then subtracted from the end time point after BVdU selection or in the untreated arm (day 16) to determine the relative enrichment of each individual sgRNAs in the BVdU arm vs. untreated arm over time. The subtracted  $\text{Log}_2$  normalized reads of the BVdU arm (day 16) vs. the untreated arm (day 16) were then analyzed using Hypergeometric and STARS analysis comparing the average of the BVdU treated samples at day 16 vs. the average of the untreated samples at day 16. Analysis of the individual replicates were also performed each yielding similar results to the average of both biological replicates. Apron analysis was also performed using the normalized counts of replicates 1 and 2 of the BVdU treated samples at day 16 compared to the average of the untreated samples at day 16. Apron, Hypergeometric, and the STARS analyses were done using the GPP web portal (<https://portals.broadinstitute.org/gpp/screener/>). The averaged data from 2 biological replicates were used for all analyses shown in the manuscript.

### sgRNA cloning to make lentiviruses

sgRNA sequences were designed using the Broad Institute sgRNA designer tool (<http://portals.broadinstitute.org/gpp/public/analysis-tools/sgrna-design>) for the DCK sgRNA rescue experiment or sgRNA sequences were used from the Brunello sgRNA library. All oligos were synthesized by IDT technologies. The sense and antisense oligonucleotides were mixed at equimolar ratios (0.25 nmol of each sense and antisense oligonucleotide) and annealed by heating to  $100^\circ\text{C}$  in annealing buffer (1X annealing buffer 100 mM NaCl, 10 mM Tris-HCl, pH 7.4) followed by slow cooling to  $30^\circ\text{C}$  for 3 h. The annealed oligonucleotides were then diluted at 1:400 in 0.5X annealing buffer.

For CRISPR-Cas9 knockout experiments in cells, the annealed oligos were ligated into LentiCRISPRV2-Puro (Addgene # 98290) or lentiCRISPRV2-Neo (Addgene #98292 where the puromycin resistance gene was replaced with the G418 resistance gene) for experiments where double knockout is needed. Ligations were performed with T4 DNA ligase for 2 h at  $25^\circ\text{C}$ . The ligation mixture was transformed into HB101 competent cells. Ampicillin-resistant colonies were screened by restriction digestion of miniprep DNAs and subsequently validated by DNA sequencing.

All following sgRNA oligos (including the BsmBI sites) used in the study to clone into the LentiCRISPR V2-Puro vector or the LentiCRISPR V2-Neo vector for CRISPR knockout experiments are listed in [Table S7](#).

### Lentivirus production

Lentiviruses were made by Lipofectamine 2000-based co-transfection of 293FT cells with the respective lentiviral expression vectors and the packaging plasmids psPAX2 (Addgene #12260) and pMD2.G (Addgene #12259) in a ratio of 4:3:1. Virus-containing supernatant was collected at 48 and 72 h after transfection, pooled together (15 mL total per 10-cm tissue culture dish), passed through a  $0.45\text{-}\mu\text{m}$  filter, aliquoted, and frozen at  $-80^\circ\text{C}$  until use.

### Lentiviral infection

For single knock-out, cells were counted using a Vi-Cell XR Cell Counter (Beckman Coulter) and  $2 \times 10^6$  cells were resuspended in 1 mL lentivirus with  $8\text{ }\mu\text{g}/\text{mL}$  polybrene in individual wells of a 12 well plate. For double knock out experiments,  $4 \times 10^6$  cells were infected using 1 mL of mixed 1:1 sgRNA #1 and #2 targeting BICRA (puromycin resistant) and/or 1 mL of mixed 1:1 sgRNA #1 and #2 targeting BICRAL (G418 resistant) and/or 1 mL of the sgControl #1 guide (2 separate constructs that were puromycin or G418 resistant) with  $8\text{ }\mu\text{g}/\text{mL}$  polybrene in individual wells of a 6 well plate. The plates were then centrifuged at 2000 rpm ( $931 \times g$ ) for 2 h at  $30^\circ\text{C}$  (Allegra X-15R Centrifuge (Beckman Coulter), rotor SX4750A). 16 h later the virus was removed and cells were grown for 72 h before being placed under drug selection. Cells were selected in puromycin ( $0.25\text{ }\mu\text{g}/\text{mL}$ ) or G418 ( $500\text{ }\mu\text{g}/\text{mL}$ ).

### Pharmacological inhibitors

The following chemicals (stored at  $-20^\circ\text{C}$  or  $-80^\circ\text{C}$ ) were added to cell culture where indicated: BVdU was purchased from Chem-Impex International Inc., catalog no. 27735. FHD-609, FHD-286, AU-15330, and dTAG-V1 were all resynthesized by Dr. Jun Qi's laboratory according to the literature. XHC-640, WA-68-VQ71, dBRD9A, BRM014 were all synthesized by Novartis and obtained under an MTA. For immunoblot analysis, the cells were treated with the drugs at the concentrations and times indicated. For dose response assays, the cells were treated with drugs at the indicated concentrations for 6 days. For dTAG-V1 experiments, the cells were treated at 100 nM overnight. For drug treatment studies, NCI-H1048, NCI-H211, COR-L311, and NCI-H526 were seeded at 100,000 cells per mL and were treated with either DMSO, 100 nM FHD-286, or 100 nM FHD-609 for 72 h. Cells were then harvested for downstream analyses.

### Cell proliferation assays

For proliferation assays with NCI-H1048 SCLC CRISPR-inactivated cells in [Figure 2](#), cells were counted on day 0 using a Vi-Cell XR Cell Counter and plated in a tissue culture-treated 6-well plate at 15,000 cells/mL for all experiments (or 30,000 cells/mL for [Figure 2H](#)) in 2 mL of complete media. Cells were trypsinized 3 or 6 days later to make single cell suspensions and were counted using a Vi-Cell XR Cell Counter (Beckman Coulter). Cell counts were then normalized to the number of cells plated at day 0.

For long-term proliferation experiments with human POU2F3-positive SCLC cell lines in [Figure S3](#), cells were counted on day 0 using a Vi-Cell XR Cell Counter (Beckman Coulter) and plated in a tissue culture-treated 6-well plates at 20,000 cells/mL in 2 mL of complete media containing XHC-640 (100 nM), WA-68-VQ71 (100 nM), dBRD9A (100 nM), or DMSO. Cell counts were performed every 3 days using the Vi-Cell until day 12. Fresh drug in fresh complete media was replaced every 3 days.

### Dose response assays

For dose-response assays, cells were counted as described above and plated in tissue culture-treated 6-well plates at 20,000 cells/mL in 2 mL of complete media. For dose-response experiments performed in ASCL1- and NEUROD1-expressing cell lines, cells were counted as described above and plated in a tissue culture-treated 6-well plates at 50,000 cells/mL in 2 mL of complete media. For all dose response assays, cells were treated with the indicated drugs at 0 nM, 0.1 nM, 1 nM, 10 nM, 100 nM, 1000 nM and after 6 days were trypsinized to make single cell suspensions and counted. Cell counts were then normalized to the DMSO condition. EC50's were calculated using non-linear regression  $\log(\text{inhibitor})$  vs. response – Variable slope (four parameters).

### Crystal violet staining

NCI-H1048 POU2F3-DCK\*-P2A-GFP cells were first transduced with lentiviruses encoding 2 independent POU2F3 sgRNAs or a non-targeting sgRNA as a control (sgControl), selected with puromycin, and counted using a Vi-Cell XR Cell Counter and plated in a tissue culture-treated 6 well plates at 40,000 cells/mL in 2 mLs of complete media. Media was replaced with fresh media every 3 days 9 days later the cells were washed twice in PBS to remove non-adherent cells and then stained with crystal violet for visualization of the entire well. Representative images were acquired using brightfield microscopy with a 10X objective.

### Immunoblotting

Cell pellets were lysed in a modified EBC lysis buffer (50 mM Tris-Cl pH 8.0, 250 mM NaCl, 0.5% NP-40, 5 mM EDTA) supplemented with a protease inhibitor cocktail (Complete, Roche Applied Science, #11836153001) and phosphatase inhibitors (PhosSTOP Sigma #04906837001). Soluble cell extracts were quantified using the Bradford Protein Assay. 20  $\mu$ g of protein per sample was boiled after adding 3X sample buffer (6.7% SDS, 33% Glycerol, 300 mM DTT, and Bromophenol Blue) to a final concentration of 1X, resolved by SDS-PAGE using either 10% or 8% SDS-PAGE, semi-dry transferred onto nitrocellulose membranes, blocked in 5% milk in Tris-Buffered Saline with 0.1% Tween 20 (TBS-T) for 1 h, and probed with the indicated primary antibodies overnight at 4°C. Membranes were then washed three times in TBS-T, probed with the indicated horseradish peroxidase conjugated (HRP) secondary antibodies for 1 h at room temperature, and washed three times in TBS-T. Bound antibodies were detected with enhanced chemiluminescence (ECL) western blotting detection reagents (Immobilon, Thermo Fisher Scientific, #WBKLS0500) or Supersignal West Pico (Thermo Fisher Scientific, #PI34078). The primary antibodies and dilutions used were: Rabbit Anti-POU2F3 (Cell Signaling #92579S, 1:1000), Rabbit Anti-ASCL1 (Abcam #Ab211327, 1:1000), Rabbit Anti-NEUROD1 (EPR4008) (Abcam #Ab109224, 1:1000), rabbit anti-DCK (Abcam #Ab151966, 1:2000), Rabbit anti-BRD9 (E9R2I) (Cell Signaling #58906, 1:1000), Rabbit Anti-BRD7 (D9K2T) (Cell Signaling #15125, 1:1000), Rabbit Anti-SMARCD1 (E7W9W) (Cell Signaling #35070, 1:1000), Rabbit Anti-BICRA (E613A) (Cell Signaling #45441, 1:1000), Rabbit Anti-BICRAL (GLTSCR1L) (Thermo Fisher Scientific #PA5-56126, 1:1000), Rabbit Anti-OCA-T1 (Cell Signaling #20217, 1:1000), Rabbit Anti-SMARCA2 (BRM) (D9E8B) (Cell Signaling #1966, 1:1000), Rabbit Anti-SMARCA4 (BRG1) (D1Q7F) (Cell Signaling #49360, 1:1000), Rabbit Anti-HA (C29F4) (Cell Signaling #3724T, 1:1000) or Mouse Anti-HA.11 (16B12) (Biolegend #901533), Rabbit Anti-GSPT1 (Abcam #Ab49878, 1:1000), Rabbit Anti-ACTL6B (E5X8C) (Cell Signaling #46787S, 1:1000), mouse  $\alpha$ -INSM1 (Santa Cruz, #SC377428, 1:1000), Rabbit Anti-Synaptophysin (YE269) (Abcam #ab32127), Rabbit Anti-Cleaved Caspase3 (Asp175) (5A1E) (Cell Signaling #9664S, 1:1000), Mouse Anti-TBP (ThermoFisher #MA1-21516, 1:1000), Rabbit Anti-ARID1A (Cell Signaling #12354, 1:1000), Mouse Anti-ARID2 (ThermoFisher #MA5-27862), Rabbit Anti-SMARCC2 (Cell Signaling #12760, 1:1000), Goat Anti-SMARCC1 (Santa Cruz Bio #sc-9746, 1:500), Mouse Anti-SMARCD2 (Santa Cruz Bio #sc-101162, 1:500), Recombinant Anti-SMARCD2 (Abcam #ab220164, 1:1000), Mouse Anti-SMARCD1 (Santa Cruz Bio #sc-135843, 1:500), Mouse Anti-ACTL6A (Santa Cruz Bio #sc-137062, 1:500), Rabbit Anti-SMARCB1 (Cell Signaling #91735, 1:1000), Mouse Anti-PBRM1 (Cell Signaling #81832, 1:1000), Mouse Anti-DPPF2 (Santa Cruz Bio #sc-514297), Mouse Anti- $\beta$ -actin (Sigma, clone AC-15, #A3854, 1:25,000) and Mouse Anti-Vinculin (Sigma, Clone hVIN-1, #V9131, 1:1000). The secondary antibodies and dilutions were: Goat Anti-Mouse (Jackson ImmunoResearch #115-035-003) and Goat anti-Rabbit (Jackson ImmunoResearch #111-035-003) and used at 1:5000. Quantitation of immunoblot band intensities of POU2F3/ $\beta$ -actin in [Figure S3A](#) were performed using ImageJ software.

### RNA-sequencing

For FHD-286 and FHD-609 experiments, 10 million cells were harvested in biological triplicate and resuspended in 1 mL of TRIzol Reagent (ThermoFisher). RNA was extracted following factory protocols. 5  $\mu$ g of RNA was then treated with DNase to remove possible genomic DNA contamination using the DNA-free DNA Removal Kit (ThermoFisher) following factory protocols. 1  $\mu$ g of

DNase-treated RNA was then used for NEB Next Poly(A) mRNA isolation and subsequent next generation sequencing library construction (NEB) following factory procedures. ERCC spike-in (Invitrogen) was added at a ratio of 2  $\mu$ L of spike-in per 1  $\mu$ g of RNA.

For WA-68-VQ71 and BRM014 experiments, NCI-H1048, NCI-H211, NCI-H526 and COR-L311 cells were plated at 200,000 cells/mL and treated with the small molecules indicated for 3 days in two independent biological replicates. RNA was extracted using RNeasy mini kit (Qiagen #74106) including a DNase digestion step according to the manufacturer's instructions and RNA-seq was performed as described below. Total RNA samples in each experiment were submitted to Novogene Inc. The libraries for RNA-seq are prepared using NEBNext Ultra II non-stranded kit. Paired end 150 bp sequencing was performed on Novaseq6000 sequencer using S4 flow cell. Sequencing reads were mapped to the hg38 genome by STAR. Statistics for differentially expressed genes were calculated by DESeq2.

### ATAC-sequencing

100,000 cells were used for the OMNI-ATAC protocol.<sup>59</sup> Cells harvested and subsequently washed once with room temperature PBS and ice-cold PBS. Cell pellets were lysed in 50  $\mu$ L cold resuspension buffer (10 mM Tris-HCl pH 7.5, 10 mM NaCl, and 3 mM MgCl<sub>2</sub>) supplemented at a final concentration of 0.1% NP40, 0.1% Tween 20, and 0.01% Digitonin for 3–5 min. Lysis step was quenched with 1 mL of resuspension buffer supplemented at a final concentration of 0.1% Tween 20 and nuclei were pelleted at 500 g for 10 min at 4°C. Nuclei were then resuspended in 50  $\mu$ L transposition reaction mix containing 25  $\mu$ L 2X Tagment DNA buffer (Illumina), 2.5  $\mu$ L Tn5 transposase (Illumina), 16.5  $\mu$ L 1X PBS, 0.5  $\mu$ L 1% Digitonin (final 0.01% v/v), 0.5  $\mu$ L 10% Tween 20 (final 0.1% v/v), and 5  $\mu$ L nuclease-free water. The transposition reaction was incubated at 37°C for 30 min with constant shaking (1000 rpm) on a thermomixer. Tagmented DNA was purified using the MinElute Reaction Cleanup Kit (Qiagen).

### ChIP-sequencing studies

Cells were crosslinked at 0.8% PFA for 10 min at room temperature. After crosslinking reactions were quenched with 150 mM glycine for 10 min at room temperatures. Cells were washed twice with ice-cold PBS and then either flash frozen in liquid nitrogen or resuspended in cell lysis buffer (50 mM HEPES pH7.5, 90 mM KCl, 1 mM EDTA, 10% Glycerol, 0.5% NP-40, 0.25% Triton X-100) for 15 min. Cell mixtures were dounced with a tight fitting glass dounce with 20–30 strokes. Nuclei were washed twice with ice-cold MNase Buffer (50 mM HEPES pH7.5, 1 mM CaCl<sub>2</sub>, 20 mM NaCl). The nuclei were then resuspended at ~10–20 million nuclei per mL of sonication buffer (50 mM, 1 mM CaCl<sub>2</sub>, 140 mM NaCl, 5 mM EDTA, 2.5 mM EGTA, 0.1% sodium deoxycholate, 0.4% sodium lauroyl sarcosinate) and added into 1 mL milliFiber Covaris tubes. Sonication was performed at 140 PIP, 6.0% DF, and 200 CPB at a rate of 60 s ON/30 s off for 10–16 cycles depending on the cell line. After sonication, sonicated chromatin was supplemented to final concentration of 1.1% Triton X- and 5% glycerol and subsequently set up for immunoprecipitation with the following antibodies: Rabbit Anti-POU2F3 (Cell Signaling E5N2D, #36135, 1.5  $\mu$ g), Rabbit Anti-BRD9 (Cell Signaling E4Q3F, #48306, 6  $\mu$ g), Rabbit Anti-ARID1A (Cell Signaling D2A8U #12354, 6.5  $\mu$ g), Recombinant Anti-BRG1 (Abcam #ab110641, 6  $\mu$ g), Rabbit Anti-SS18 (Cell Signaling D6I4Z #21792, 2.5  $\mu$ g), Rabbit Anti-H3K27ac (Cell Signaling D5E4 #8173, 30 ng), and Mouse Anti-RPB1 (Cell Signaling 4H8 #2629, 2  $\mu$ g).

IPs were performed overnight at 4°C and then incubated with animal-specific dynabeads (ThermoFisher) for 2.5 h at 4°C. Beads were washed 3X with RIPA150 (10 mM Tris HCL pH7.5, 1 mM EDTA, 0.1% sodium dodecyl sulfate, 0.1% sodium deoxycholate, 1% Triton X-100, 150 mM NaCl), then 3X with RIPA500 (10 mM Tris HCL pH7.5, 1 mM EDTA, 0.1% sodium dodecyl sulfate, 0.1% sodium deoxycholate, 1% Triton X-100, 500 mM NaCl), and 3X with LiCl Wash Buffer (250 mM LiCl, 0.5% NP-40, 0.5% sodium deoxycholate). Beads were then eluted with ChIP Elution Buffer (50 mM Tris HCL pH 7.5, 10 mM EDTA, 1% sodium dodecyl sulfate) and reverse crosslinked with proteinase K overnight at 65°C and subsequently treated with RNase A (NEB) for 1 h at 37°C. ChIP DNA was purified using Qiagen MinElute Reaction Cleanup kit (Qiagen) following factory protocols.

### ChIP-Rx

ChIP-Rx used the previously described ChIP-seq with a few modifications following the Orlando et al. method.<sup>61</sup> Briefly, S2 cells were crosslinked and sonicated following the ChIP-seq protocols. For spike-in ratio, 1  $\mu$ g of *Drosophila* spike-in chromatin was added to 40  $\mu$ g of target chromatin per immunoprecipitation. For antibody amount 0.5  $\mu$ g of H2Av antibody (Active Motif #61571) was added to each ChIP-Rx experiment. Post spike-in antibody and chromatin addition followed ChIP-seq protocol exactly.

### Co-immunoprecipitation experiments

POU2F3, BRD9, and ARID1A co-immunoprecipitation studies were performed as follows. Cells were washed with PBS twice and then immediately lysed for nuclei with hypotonic buffer (10 mM Tris-HCl, 15 mM KCl, and 1 mM MgCl<sub>2</sub>) supplemented with proteinase inhibitors and 1 mM DTT. Samples were spun gently at 500 xg for 10 min at 4°C to collect nuclei. Nuclei were then lysed with EB150 (50 mM Tris-HCl pH 7.5, 150 mM NaCl, 1% Triton X-, 1 mM EDTA, 1 mM MgCl<sub>2</sub>, 0.1% Na Deoxycholate) supplemented with proteinase inhibitors and 1 mM DTT. Lysates were incubated at 4°C for 30 min and spun down at 15000 xg at 4°C for 10 min. 2 mg of protein were used for each immunoprecipitation experiment with 8.0  $\mu$ g of BAF antibodies [anti-ARID1A (CST D2A8U) and anti-BRD9 (CST E4Q3F)] or IgG (abcam ab172730) or 5.0  $\mu$ g of POU2F3 antibody (CST E5N2D). Antibody with lysates were incubated overnight at 4°C and then incubated with sheep anti-rabbit Dynabeads (Invitrogen) for 3 h at 4°C. Antibody-dynabead slurries were washed with EB150 6x, eluted with 2X LDS with 100 mM DTT, and subsequently loaded into SDS-PAGE gels for Western blotting.

### Exogenous POU2F3 and OCA-T2 rescue experiments

For HA-dTAG-POU2F3 or OCA-T2-dTAG-HA system, the FKBP23F36V-2xHA was PCR amplified from the pCRIS-PITChv2-Puro-dTAG vector (addgene #91703) and introduced into sgRNA-resistant POU2F3\_LentiV\_NEO or the OCA-T2\_LentiV\_neo vector for functional validation with competition-based cell proliferation assay. NCI-H1048 cells that stably expressed Cas9 were infected either with HA\_dTAG\_POU2F3\_LentiV\_neo or OCA-T2\_dTAG\_HA\_LentiV\_neo or empty\_vector\_lentiV\_neo construct followed by neomycin selection to establish stable cell lines. The cells were then lentivirally delivered with indicated sgRNAs co-expressed with a GFP reporter. The percentage of GFP+ cells corresponding to the sgRNA representation within the population. GFP measurements in human cell lines were taken on day 4 post-infection and every four days with Guava EasyCyte HT instrument (Millipore). The fold change in GFP+ population (normalized to day 4) were used for analysis. After validating the functionality of tagged POU2F3/OCA-T2, the HA\_dTAG\_POU2F3 or OCA-T2\_dTAG\_HA, which is linked with blasticidin resistant gene through P2A linker (HA\_dTAG\_POU2F3\_P2A\_blasticidin, or OCA-T2\_dTAG\_HA\_P2A\_Blasticidin) and resistant to its own sgRNA, were cloned into the LRG2.1T vector that either contains sgRNA against endogenous POU2F3 or OCA-T2 into NCI-H1048 that stably express Cas9. The following sgRNA oligos were used for CRISPR knockout: sgControl #1 = AGTCGCTTCTCGATTATGGG, sgControl #2 = CAGAGTCTCCTATGC CACAC, sgCDK1 = ACACAATCCCCTGTAGGATT, sgPOU2F3 #4 = GACCAACATCCGCCTGACTC, sgOCA-T2 #1 = CGGACACCT TGATACACCTT and sgOCA-T2 #2 = CCGAGTGAAGATCACAGTGA.

For immunoblot analyses in NCI-H1048 cells expressing HA-dTAG-POU2F3, or HA-dTAG-OCA-T2, or parental NCI-H1048 cells, cells were plated at 200,000 cells/mL and treated with the small molecules indicated for 3 days. For the dose response assays, the cells were plated at 20,000 cells/mL and treated with the small molecules indicated for 6 days and counted using the Vi-Cell. Cell counts were then normalized to the number of cells plated at day 0. EC<sub>50</sub>'s were calculated using non-linear regression log(inhibitor) vs. response-variable slope (four parameters).

### Reverse-transcriptase quantitative PCR (RT-qPCR)

RNA was extracted using Quick-RNA Miniprep kit (Zymo Research, CA, USA) according to the manufacturer's instructions. RNA concentration was determined using the Nanodrop 8000 (ThermoFisher Scientific). A cDNA library was synthesized using iScript Reverse Transcription Supermix for RT-qPCR (Biorad #1708841) according to the manufacturer's instructions. qPCR were performed using the LightCycler 480 (Roche) with the LightCycler 480 Probes Master Kit (Roche) and Taqman probes (ThermoFisher Scientific) according to the manufacturer's instructions. The  $\Delta\Delta C_T$  Method was used to analyze data. The C<sub>T</sub> values for each probe were then normalized to the C<sub>T</sub> value of *ActB*. The following TaqMan probes were used: *ACTB* human (Hs01060665\_g1), *POU2F3* human (Hs00205009\_m1), *ASCL1* human (Hs04187546\_g1), *NEUROD1* human (Hs00159598\_m1), *OCA-T1* (*C11ORF53*) human (Hs00736612\_m1), *COLCA2* (OCA-T2) human (Hs00416978\_m1), *INSM1* human (Hs00357871\_s1), *SYP* human (Hs00300531\_m1) and *CHGA* human (Hs00154441\_m1). For Figure 8J, MGH1521-1A #1 and #2 PDXs are from the vehicle-treated tumors and the cell line xenografts are from a vehicle treated tumor in Figure 8B (NCI-H1048) or from untreated mice (NCI-H526, COR-L311).

### Small cell lung cancers cell line xenografts and treatment studies

For NCI-H1048 and NCI-H211 xenografts, parental cells were grown to 10<sup>9</sup> cells, washed 3 times in 50 mLs of sterile PBS, and resuspended at 6 × 10<sup>7</sup> cells/mL in PBS with 50% Matrigel (Westnet Inc. #356231) for NCI-H1048 xenografts or resuspended at 10 × 10<sup>7</sup> cells/mL in PBS with 50% Matrigel (Fisher Scientific #CB40234) for NCI-H211 xenografts. The mice were anesthetized with isoflurane and 6 × 10<sup>6</sup> cells (for NCI-H1048) or 10 × 10<sup>6</sup> cells (for NCI-H211) were injected subcutaneously into bilateral flanks of 6-week-old NCr nude female mice (Taconic #NCRNU) and were monitored daily. For NCI-526 and COR-L311 xenograft controls shown in Figure 8J, cells were prepared and injected as described above for NCI-H1048 cells.

For the pharmacodynamic (PD) study and efficacy study in Figures 8A–8H, when subcutaneous flank tumors were on average ~100 mm<sup>3</sup> in size (~2 weeks after injection), mice were randomized to treatment with either FHD-609, FHD-286, or vehicle (HP-β-CD, Sigma Aldrich #778966). Vehicle was first made by resuspending HP-β-CD at 20% in UltraPure Distilled Water (Thermo Fisher Scientific #10977023). FHD-609 and FHD-286 powder were weighed using a high precision scale (Mettler Toledo, XS105), resuspended in the HP-β-CD vehicle and rotated overnight at 4°C. All drugs, including vehicle, were made fresh twice a week and stored in the dark at 4°C. FHD-609 was dosed daily at 0.5 mg/kg by intraperitoneal (IP) injections. Vehicle was also dosed daily by IP injections. FHD-286 was dosed daily at 1.5 mg/kg by oral gavage (PO). For the PD study, mice were dosed daily for 7 days and tumors were harvested 6 h after the last dose and flash frozen (2/3) or fixed (1/3) for downstream analysis. For the efficacy study, mice were dosed continuously for 35 days at which time they were monitored off treatment until each mouse reached its endpoint. All mice with tumors were enrolled and no data were excluded. Tumor diameters were measured twice a week using calipers until mice were euthanized and tumor volume was calculated using: tumor volume (mm<sup>3</sup>) = (width)<sup>2</sup> × length/2. Body weights were also measured twice a week to monitor for overt toxicity. Mice were euthanized when one of the tumors reached their endpoint of >1500 mm<sup>3</sup>. In the NCI-H211 xenograft experiment, there was 1 mouse in the FHD-286 arm and 1 mouse in the vehicle arm that had a tumor that didn't grow following treatment completion. All mice were followed up until 70 days at which point all other mice reached their endpoint except for the 2 mice above. At this point, the study was ended and both of these mice were also euthanized. The Kaplan Meier Estimator was performed to analyze median overall survival. Upon euthanasia, ~2/3 of each lung tumor was immediately flash frozen on dry ice for subsequent RNA and protein analysis, ~1/3 of each lung tumor was fixed in 10% formalin for 24 h then stored in 70% ethanol before being embedded in paraffin.

For the chemotherapy combination study, when subcutaneous flank tumors were on average  $\sim 150 \text{ mm}^3$  in size, mice were randomized to treatment with either FHD-609, FHD-286, cisplatin/etoposide, or vehicle (HP- $\beta$ -CD, Sigma Aldrich #778966) alone, or the combination of FHD-609 or FHD-286 with cisplatin/etoposide. FHD-609 and FHD-286 were prepared and dosed as described above. Cisplatin (Fresenius Kabi, #100365) and Etoposide (Novaplus/Hikma Pharmaceuticals USA, #0143-9376-01) were dosed at 5 mg/kg on day 1 and 8 mg/kg on days 1,2, and 3, respectively, by IP injection every 14 days beginning 3 days after treatment initiation with FHD-609, FHD-286, or vehicle. Cisplatin/etoposide was given for a total of 3 cycles (days 3,17,31 after treatment initiation). Mice were treated continuously for 45 days. All mice with tumors were enrolled, but tumors  $< 80 \text{ mm}^3$  at the start of the treatment were excluded. Tumor and mouse body weights measurements were performed as described above.

### Patient-derived xenografts and treatment studies

Efficacy studies for the SCLC PDX MGH1521-1A were performed largely as described above for NCI-H1048 and NCI-H211, with the following amendments. First, xenografts were generated by direct implantation of resected xenograft fragments into the right flanks of NSG mice (NOD.Cg-Prkdc<sup>scid</sup> Il2rg<sup>tm1Wjl</sup>/SzJ). Second, treatment studies were initiated when flank tumors reached 200–400  $\text{mm}^3$  in size, as calculated above. Third, mice were treated until endpoints of xenograft volume exceeding 3x initial tumor volume or 30 days after start of treatment, whichever was reached first. All PDX studies were conducted through Institutional Animal Care and Use Committee-approved animal protocols in accordance with University of Texas Southwestern Medical Center institutional guidelines.

### Data analysis

#### Data processing for RNA sequencing, ATAC-seq, and ChIP-Seq

RNA-seq and ATAC-seq samples were demultiplexed using bcl2fastq v2.20.0.422. The sequenced RNA-seq reads were aligned to hg19 assembly with STAR v2.5.2b.<sup>62</sup> The sequenced ATAC-seq reads were first trimmed with Trimmomatic v0.36, aligned with Bowtie2 v2.2.9, and filtered with Picard v2.8.0 (MarkDuplicates REMOVE\_DUPLICATES = true) and SAMtools v 0.1.19 (-F 256 -f 2 -q 30).<sup>57,63,64</sup> Reads mapping to regions defined in the ENCODE project's wgEncodeDacMapabilityConcensusExcludeable bed file were removed using bedtools v2.30.0.<sup>65</sup> The sequenced ChIP-seq reads were processed identically to ATAC-seq reads. All genomics data (ATAC-seq, RNA-seq, and ChIP-seq) have been deposited to the Gene Expression Omnibus (GEO) under accession number: GSE249362 except RNA-seq data of cells treated with BRM014 and WA-68-VQ71 are in GEO under accession number GSE249258. Data will be released upon publication.

#### ATAC-seq analysis

ATAC reads were merged across technical replicates using samtools merge.<sup>57</sup> Reads were filtered to only include reads with an insert size of 38–100 bp, pre-shift, using htlib.<sup>66</sup> Peaks were called using MACS3 callpeak (-q 0.01 -nomodel -extsize 200).<sup>58</sup> Venn diagrams of peak overlaps were generated using bedtools intersect, and visualized using the eulerr R package.<sup>65,67</sup> PCA plots for ATAC were plotted using the top 500 peaks by variance. Counts were determined using bedtools intersect, then variance stabilizing transformation was applied. FASTA sequences across given sites were generated using site centers with flanking windows of 200 bp (total window size of 400 bp). Enriched motifs across these sets of sites were determined using HOMER findMotifsGenome.pl against genome-background (-size 400).<sup>68</sup> HOMER motif known results were visualized as barplots using ggplot2. Heatmaps and metaplots were generated over indicated peaks using deepTools computeMatrix.<sup>69</sup> Bigwig inputs for heatmaps were generated with deepTools bamCoverage (-binSize "40" -normalizeUsing "CPM" -exactScaling).<sup>69</sup> Different sets of sites were assigned to their nearest protein-coding gene using bedtools closest. These distances were visualized as stacked bar charts using ggplot in R, highlighting the proportion of promoter, promoter proximal, and distal enhancer regions. For Figure 6J, ATAC fold-changes were determined by finding ATAC peaks in both conditions within  $\pm 10 \text{ kb}$  of the differentially expressed gene's TSS, and calculating the fold change in reads-per-million across all such peaks.

#### ChIP-seq analysis

Bigwigs were again generated using deepTools bamCoverage (-binSize "40" -normalizeUsing "CPM" -exactScaling) and visualized using IGV.<sup>70</sup> Peaks were called using MACS3 callpeak (-nomodel -extsize 200)<sup>58</sup> at a q-value threshold of 0.01, and at a q-value threshold of 0.05 SMARCA4 ChIP-seq peaks in Figures 4I and S4R only, to achieve a more similar overall peak count to other marks.

ChIP-seq reads for BRD9, POU2F3, and Input were additionally aligned to the BDGP6 assembly using Bowtie2 v2.2.9 for downstream normalization.

Gained, retained, and lost SMARCA4 peaks in each drug treatment condition were determined using a fold-change threshold of 1.5 on reads-per-million normalized read counts at each peak, counted with bedtools intersect, and visualized using venn diagrams generated using the eulerr R package.<sup>65,67</sup> FASTA sequences across given sites were generated using site centers with flanking windows of 200 bp (total window size of 400 bp). Enriched motifs across these sets of sites were determined using HOMER findMotifsGenome.pl against genome-background (-size 400).<sup>68</sup> HOMER motif known results were visualized as barplots using ggplot2. Heatmaps and metaplots were generated over indicated peaks using deepTools computeMatrix.<sup>69</sup> Bigwig inputs for heatmaps were generated with deepTools bamCoverage (-binSize "40" -normalizeUsing "CPM" -exactScaling)<sup>69</sup> for ATAC-seq reads and SMARCA4 and SS18 ChIP-seq reads. BRD9, POU2F3, and Input ChIP-seq reads were normalized by spike-in Drosophila read

counts, calculated as described previously, and scaled using the coefficients output by `deeptools multiBamSummary` divided by 100 (`-binSize 40 -normalizeUsing None -exactScaling -scaleFactor "X"`).

For **Figure 4H**, ChIP-seq reads were calculated across all SMARCA4 peaks in all cell lines, merged using `bedtools`. Reads were then normalized using the `normalize.quantiles` function in the `preprocessCore` R package.<sup>71</sup> Peaks were clustered using k-means clustering in a semi-supervised manner, merging visually similar clusters. Z-scores were computed row-wise for visualization, and a subset of genes whose transcription start site fell within a 10 kb window of a peak center were also generated as labels.

### RNA sequencing data analysis

Identification of upregulated or downregulated genes across the conditions were determined using `DESeq2`<sup>59</sup> ( $\log_2FC = 1$ , B-H  $p$ -value = 0.05). Normalized counts were generated using `DESeq2`'s `estimateSizeFactors` function. Volcano plots for changes in expression were visualized as scatterplots using `ggplot2`.<sup>72</sup> Venn diagrams of differential genes were generated using the `eulerr` R package.<sup>65,67</sup>

PCA plots were generated using variance stabilizing transformed counts, across the top 500 genes by variance, and plotted using `ggplot2`. Heatmaps were generated using the `ComplexHeatmap` R package,<sup>60</sup> and visualize Z Score normalized read counts for each gene across all samples for each cell line, unless otherwise indicated. Hierarchical clustering was performed using Spearman or Kendall distance functions.

GSEA analysis was performed using the Hallmark gene sets, through the `msigdb` R package, using `clusterProfiler` GSEA function.<sup>73</sup> Differential expression ranking was determined by the "stat" output from `DESeq2`. For GSEA analysis in **Figures 7A, 7B, S7A, and S7B**, GSEA software was obtained from the GSEA website [<http://www.broad.mit.edu/gsea/downloads.jsp>]. Top 200 downregulated gene lists were identified as significantly downregulated genes (adjusted  $p$  value < 0.05) with top 200 log transformed fold decrease after FHD-286 or BRM014 treatment (100 nM for 72 h) on NCI-H211, NCI-H1048, NCI-H526, and COR-L311, FHD-609 or WA-68-VQ71 treatment (100 nM for 72 h) on NCI-H211 and NCI-H1048 (**Table S5**). Subsequently, pre-ranked GSEA was performed on log transformed fold change profiles from RNA-sequencing data reported in Wu et al., *Nature*, 2022,<sup>13</sup> where POU2F3, OCA-T1 or OCA-T2 was knocked out in NCI-H211, NCI-H1048, NCI-H526, and COR-L311 cell lines. For **Figure 7C**, genes downregulated in half or more treatment conditions were selected, and Z-scores for each replicate were calculated across each cell line for each gene.

For RNA-seq data from the George et al. paper,<sup>4</sup> FPKM values from all tumors were analyzed across all tumors ( $n = 81$ ) to first select tumors that highly expressed POU2F3 (high = FPKM values > 2) which contained 12 tumors. 2 POU2F3-positive tumors (S01297 and S02375) had dominant expression of ASCL1 or NEUROD1 relative to POU2F3 and hence were excluded as potential confounders as ASCL1 and NEUROD1 positive tumors are associated with higher neuroendocrine gene expression. For **Figure S4D**, principal component analysis was conducted on RPKM values for SCLC-P samples from George et al. 2015<sup>4</sup> using the top 500 NE-signature genes from Balanis et al. 2019,<sup>46</sup> and clusters were identified using SYP, INSM1, and CHGA expression. Loadings for PC1 (**Figure S4E**) were calculated from the rotation vector output by R's "prcomp" function.

For **Figures S4G–S4I**, RNA expression data and multi-omics cluster annotations from the Tonji University SCLC cohort was obtained from Liu et al. 2024.<sup>47</sup> Log<sub>2</sub>p1-transformed TPM was plotted for each transcriptional subtype-defining driver for each cluster, and all samples in multiomics cluster `nmf4` were considered as SCLC-P cases by POU2F3 expression. Principal component analysis was conducted on SCLC-P samples using the top 500 NE-signature genes from Balanis et al.,<sup>46</sup> and plotted with `ggplot2`.<sup>72</sup> SCLC-P NE cases were identified by relative CHGA, SYP, and INSM1 expression.

For **Figure S5E**, primary targets were identified for differentially expressed genes whose TSS were within +/– 10 kb of a concordant change in accessibility, using `bedtools` closest and the GENCODE consortium version 44 annotation for GRCh37.

For PCA in **Figure 8K**, top 500 genes with the largest standard deviation of TPM values were subjected to principal component analysis using the `removeBatchEffect` function in the `limma` package (version 3.58.1) and `prcomp` function of R software (version 4.3.3).

### Correlation analyses of validated enriched screen hits with POU2F3 dependency or POU2F3 expression

Correlation of SMARCD1, BRD9, EP300, MED19, IPPK, and KAT7 dependencies with POU2F3 dependency or POU2F3 expression was analyzed using gene effect from publicly available data from DepMap (DepMap Public 23Q2+Score, Chronos).<sup>40</sup> For **Figure 2**, all POU2F3-positive SCLC cells (NCI-H1048, NCI-H211, NCI-H526, and CORL-311) were compared to all other SCLCs ( $n = 23$  SCLC cell lines in total with 4 POU2F3-positive SCLCs and 19 other SCLCs), and then compared to all other cancer cell lines in the dependency map. For **Figure S2**, only SCLC cell lines were included ( $n = 23$ ) and were binned by POU2F3 expression as above.

### SMARCD1, BRD9 and BAF complexes gene effect calculations

DepMap Public 23Q2 CRISPR based gene effect estimates for all models in the Achilles pipeline, integrated using `Harmonia`, were downloaded from the DepMap portal (<https://depmap.org/portal/>). POU2F3-positive SCLCs ( $n = 4$ ) were compared to all other SCLCs ( $n = 19$ ), and then compared to all other cancer cell lines. Gene effect for each BAF complex, in **Figure S2B**, was calculated based on BAF subunits reported in Michel et al., *Nature Cell Biology*, 2018<sup>39</sup> (see **Table S3** for gene list). If paralogs were present in the complex, their gene effects were first averaged then the paralog average was included before averaging with all other unique subunits in the complex.

## QUANTIFICATION AND STATISTICAL ANALYSES

For the *in vivo* xenograft studies in [Figures 8E–8H](#), [S8B](#), and [S8D](#), both raw tumor volumes and log tumor fold-change normalized to day 0 are shown. The tumor volume fold-changes were log-transformed to stabilize the variability across time points. Log tumor fold-changes were modeled over the duration of treatment (until day 35) using a linear mixed-effects model accounting for the repeated measures within each tumor. The model included time (days), arm (FHD-609, FHD-286, and vehicle control), and the interaction between time and arm as covariates; these interaction terms evaluated the differences in the rate of change of the log tumor fold-change over time between arms and were considered significant at the 0.10 level. Survival was evaluated using Kaplan-Meier curves, and Gehan-Breslow-Wilcoxon tests were used to compare survival curves between arms as treatment only occurred during the first 35 days of the study and thereafter mice were monitored off treatment for survival. *p*-values of <0.05 were considered statistically significant.

For the combination efficacy studies with cisplatin/etoposide chemotherapy in [Figures S8J–S8L](#), log fold-change tumor volumes normalized to day 0 are shown. Log fold-change in tumor volume were modeled over the duration of treatment (until day 45) using a linear mixed-effects model accounting for the repeated measures within each tumor. The model included time (days), arm (Vehicle control arm, FHD-609 or FHD-286, cisplatin/etoposide, and the corresponding combination of FHD-609 or FHD-286 with cisplatin/etoposide), and the interaction between time and arm as covariates; these interaction terms evaluated the differences in the rate of change of the log fold-change in tumor volume over time between arms. Tumors with starting volumes less than 80 mm<sup>3</sup> were excluded from the analysis. Additive effect of the drugs with chemotherapy was calculated using a test of equality between the sum of the cisplatin/etoposide alone and FHD-609 or FHD-286 alone average treatment effects (i.e., sum of the difference between cisplatin/etoposide vs. vehicle slopes and the difference between FHD-609 or FHD-286 vs. vehicle slopes) and the average treatment effect for the combination arm (i.e., the difference between the combination vs. vehicle slopes). Contrast estimates from the linear mixed effects models were then used to compare the observed combination treatment effects with the expected individual treatment effects. The difference between the observed and expected average combination treatment effect was 0.009 (95% CI: –0.013, 0.031) for FHD-286 and 0.012 (95% CI: –0.012, 0.035) for FHD-609. The confidence intervals for these comparisons of the observed vs. expected combination treatment effects for each FHD-609 + cisplatin/etoposide and FHD-286 + cisplatin/etoposide included 0, supporting the conclusion that the actual combination effect was close to the predicted one. This allows to conclude that the individual treatments within the combinations FHD-609 + cisplatin/etoposide and FHD-286 + cisplatin/etoposide were additive.

For screen replicate reproducibility, *r* Pearson correlation coefficient's were calculated and included in [Figures S1H](#) and [S1I](#). For the positive-selection BVdU resistance CRISPR screen analysis, Apron, Hypergeometric, and STARS analyses were performed and included in [Table S2](#). For all other experiments, statistical significance was calculated using unpaired, two-tailed Student's *t* test. *p*-values were considered statistically significant if the *p*-value was <0.05. For all figures, \* indicates *p*-value < 0.05, \*\* indicates *p*-value < 0.01, \*\*\* indicates *p*-value < 0.001, and \*\*\*\* indicates *p*-value < 0.0001. Error bars represent mean ± SEM unless otherwise indicated.